

Development of a Transmission-type Ultra-thin  
ScCVD Diamond  $\Delta E$  Detector for Alpha Particles

DEVELOPMENT OF A TRANSMISSION-TYPE ULTRA-THIN  
SCCVD DIAMOND  $\Delta E$  DETECTOR FOR ALPHA PARTICLES

BY  
XINGZHI CHENG, B.Sc.

A THESIS  
SUBMITTED TO THE DEPARTMENT OF RADIATION SCIENCE  
AND THE SCHOOL OF GRADUATE STUDIES  
OF MCMASTER UNIVERSITY  
IN PARTIAL FULFILMENT OF THE REQUIREMENTS  
FOR THE DEGREE OF  
MASTER OF SCIENCE

© Copyright by Xingzhi Cheng, September 2020

All Rights Reserved

Master of Science (2020)  
(Radiation Science)

McMaster University  
Hamilton, Ontario, Canada

TITLE: Development of a Transmission-type Ultra-thin ScCVD  
Diamond  $\Delta E$  Detector for Alpha Particles

AUTHOR: Xingzhi Cheng  
B.Sc. (Medical Physics),  
McMaster University, Hamilton, Canada

SUPERVISOR: Dr. Soo Hyun Byun

NUMBER OF PAGES: xii, 112

# Abstract

We present an ultra-thin transmission-type radiation detector developed for counting microbeam alpha particles. The  $\Delta E$  alpha detector is a single crystal chemical vapor deposited diamond (ScCVDD) and will be installed between the microbeam accelerator window and a biologic sample. The commercially available optical grade ScCVDD sample ( $3 \text{ mm} \times 3 \text{ mm} \times 50 \text{ }\mu\text{m}$ ) was etched down to a few  $\mu\text{m}$  thickness which allows alpha particles to penetrate, and then it was followed by the surface cleaning, electrical contact deposition and post-metallization annealing. SRIM code and MCNP6 were used for energy loss calculation of alpha particles in electrodes and diamond and pulse height spectra prediction. In order to evaluate the performance of the ultra-thin ScCVDD detector, a  $\Delta E$ -E detectors system was set up using a calibration source, the ScCVD detector and a silicon surface barrier detector (SBD). The absolute and intrinsic totally efficiency was determined as 0.3 % and 16 % respectively. Alpha and gamma peaks were observed while the peak resolution is not quite promised. The transmission ability of the ScCVDD detector was verified by applying coincidence operation with  $0.22 \text{ }\mu\text{s}$  time window. The thickness of the ultra-thin diamond sample was reassessed to be  $8.315 \pm 0.690 \text{ }\mu\text{m}$  from  $\Delta E$ -E spectrometry.

# Acknowledgements

I have been a part of McMaster Medical Physics program for 5 years since 2015 throughout my undergrad and graduate career. For an international student who came from another side of the Pacific Ocean, words can never fully express how immensely grateful I am for all wonderful things here. I am also specially grateful for all the support during the COVID19 pandemic.

I would like to sincerely thank my supervisor, Dr. Soo Hyun Byun, for offering me such a great opportunity to work on nuclear instrumentation. Your expertise, passion and knowledge always directs, encourages and inspires me to move forward. It is my great honor and fortune to have you as my supervisor. Thanks to Dr. Alan Chen, Dr. Jeroen Thompson and Dr. Doug Boreham and Dr. Andrei Hanu for being in my committee and providing insightful comments.

Without tons of helps and collaborations from faculty of Engineering, my project will never have a chance to succeed. Deeply thanks to Dr. Shahram Tavakoli and Ms. Doris V. Stevanovic and Dr. Ross Anthony from CEDT for their patient training and reliable assistance with my detector fabrication. Appreciate Ms. Baoqin Deng from MMRI for providing optical thickness measurement. I wish to thank Mr. Josh Lawrence and Mr. Jan Boer from Learning Factory for your help on laser engraving. Also greatly thank Mr. Jim Cleaver from Engineering Machine Shop who made me

many metal parts.

Thank Mr. Justin Bennett and Mr, Scott McMaster for your technique support. I would like to have special thanks to Ms. Xin Tong for her vital helps during the first year of my research. Without the experiences you selflessly shared, it would take me much longer to be there. Thanks to everyone in Byun's group for these suggestions and helps that I always seek. Also thank all my colleagues in RadGrad, especially those in TAB 104B, for all the cheerful time with you.

I really thank my parents and my family back in China for your endless support and concern. Last but not least, please allow me to express my gratitude to Liu Yu. With your company and support, I will always be positive and fearless to the unknown future.

# Contents

<b>Abstract</b>	<b>iii</b>
<b>Acknowledgements</b>	<b>iv</b>
<b>1 Introduction</b>	<b>1</b>
1.1 A Review of Microbeam . . . . .	1
1.1.1 Introudction to Microbeam . . . . .	1
1.1.2 Beamline Formation and Vacuum Window . . . . .	4
1.1.3 Cell Recognition and Observation . . . . .	5
1.1.4 Particle Detection . . . . .	6
Pre-cell Configuration . . . . .	6
Post-cell Configuration . . . . .	8
1.1.5 Conclusion . . . . .	9
1.2 McMaster University Microbeam Facility . . . . .	12
1.3 Motivation and Objective . . . . .	13
<b>2 Chemical Vapor Deposited Diamond</b>	<b>17</b>
2.1 Physical Properties of Diamond . . . . .	18
2.1.1 Diamond Lattice . . . . .	18

2.1.2	Band Structure and Band Gap . . . . .	18
2.1.3	Lattice Vibration and Thermal Conductivity . . . . .	22
2.1.4	Transport Properties of Charge Carriers . . . . .	25
	Bloch Electron and Hole . . . . .	25
	Scattering . . . . .	27
	Charge Carriers Mobility and Drift Velocity . . . . .	28
	Electrical Conductivity and Resistivity . . . . .	29
2.1.5	Dielectrics . . . . .	30
2.2	Basics of Chemical Vapor Deposition . . . . .	32
2.3	CVD Diamond Surface and Contacts . . . . .	33
	2.3.1 Surface Termination . . . . .	33
	2.3.2 Contacts . . . . .	34
<b>3</b>	<b>Diamond as a Solid-State Particle Detector</b>	<b>38</b>
3.1	Interaction of Charged Particles . . . . .	38
3.2	Charge Carrier Generation . . . . .	41
3.3	Impurities and Dopants . . . . .	44
3.4	Trapping and Recombination . . . . .	46
<b>4</b>	<b>Fabrication of the Ultra-thin ScCVD Diamond detector</b>	<b>48</b>
4.1	Commercial ScCVD Diamond . . . . .	48
4.2	Plasma Etching . . . . .	49
4.3	Cleaning . . . . .	51
4.4	Electrodes Fabrication . . . . .	52
4.5	Electronic Assembling . . . . .	54

<b>5</b>	<b>Computational Modeling of the ScCVD diamond detector</b>	<b>56</b>
5.1	SRIM Calculation . . . . .	56
5.1.1	Method . . . . .	56
5.1.2	Results . . . . .	58
5.2	MCNP Simulations . . . . .	60
5.2.1	Introduction to MCNP . . . . .	60
5.2.2	Method . . . . .	60
	Source-CVDD-SBD configuration . . . . .	61
	Microbeam configuration . . . . .	62
5.2.3	Results . . . . .	65
	Source-CVDD-SBD configuration . . . . .	65
	Microbeam configuration . . . . .	68
<b>6</b>	<b>Characteristics Investigation</b>	<b>72</b>
6.1	Ultra-thin ScCVDD Detector Characterization . . . . .	72
6.1.1	Setup and Methodology . . . . .	72
6.1.2	Functionalities . . . . .	74
6.1.3	Trapping Phenomenon and Restoration . . . . .	80
6.2	ScCVDD-SBD $\Delta E$ -E System . . . . .	83
6.2.1	Setup and Methodology . . . . .	83
6.2.2	Coincidence Time Window . . . . .	86
6.2.3	$\Delta E$ -E Measurements . . . . .	88
6.2.4	ScCVDD Thickness Reassessment . . . . .	92
<b>7</b>	<b>Conclusion and Future Work</b>	<b>96</b>

7.1	Conclusion . . . . .	96
7.2	Future work . . . . .	98

# List of Figures

1.1	Schematic drawing of McMaster microbram facility . . . . .	14
2.1	Schematics of the diamond cubic structure . . . . .	19
2.2	Energy band formation . . . . .	20
2.3	Bnad structure and first Brillouin zone of diamond . . . . .	22
2.4	Schematic description of the CVD process . . . . .	34
2.5	Energy level diagrams for a contact between a metal and an intrinsic semiconductor . . . . .	36
4.1	Alicona surface profiles . . . . .	51
4.2	Sputtering . . . . .	53
4.3	Assembled ScCVD diamond detector . . . . .	55
5.1	Energy loss of alpha particles through Al and Cr/Au electrodes. The dash lines represent the boundary of materials . . . . .	59
5.2	MCNP configuration of CVDD/CVDD-SBD . . . . .	64
5.3	MCNP configuration of CVDD on microbeam . . . . .	65
5.4	MCNP Pulse Height Spectrum of Source-CVDD-SBD . . . . .	68
5.5	MCNP Pulse Height Spectrum of microbeam setup . . . . .	71
6.1	Source-CVDD detector setup and electronics chain . . . . .	74
6.2	Oscilloscope signals . . . . .	75

6.3	ScCVDD detector spectrum at different HVs . . . . .	76
6.4	Am-241 and Cm-244 spectrum . . . . .	79
6.5	Trapping . . . . .	81
6.6	Spectra of ScCVDD detector for long-time measurements . . . . .	82
6.7	Source-CVDD-SBD detector setup and electronics chain . . . . .	84
6.8	Time interval distribution . . . . .	87
6.9	Oscilloscope signals $\Delta E-E$ . . . . .	88
6.10	$\Delta E-E$ spectra . . . . .	90
6.11	$\Delta E-E$ coincidence . . . . .	92
6.12	SBD spectrum with and without diamond in way . . . . .	93

# List of Tables

1.1	Features of selected charged participle microbeam facilities . . . . .	10
2.1	Physical properties of selected semiconductors . . . . .	31
4.1	RIE parameters . . . . .	50
5.1	Energy loss in Source-CVDD-SBD . . . . .	66
5.2	Energy loss in microbeam setup . . . . .	69
6.1	CoMPASS parameters . . . . .	86

# Chapter 1

## Introduction

### 1.1 A Review of Microbeam

#### 1.1.1 Introduction to Microbeam

A microbeam is defined as a highly collimated or focused radiation source that only irradiate micron-sized of local area. The earliest attempt of localized irradiation was almost 110 years ago by Tchakhotine [1] by using a a few microns wide ultraviolet light beam on cells. The technique of partial irradiation had studied since that time and the source types had been developed ranging from charge particles (protons, electrons and  $\alpha$  particles) to electromagnetic radiation (X-ray and infrared wavelengths) [2]. Partial-cell irradiation technique provided tool to study radiation induced injurious effect in living system and analyze the normal function of various cell parts by selectively altering them [3]. Zirkle from University of Chicago, one of the pioneers in the field of microbeam development and application, conducted the first charged-particle microbeam (2 MeV protons and 4 MeV  $\alpha$  particles produced

from a Van de Graaff accelerator) experiment with his colleague in 1953 to study the cell division after irradiation in metaphase [3]. After 1950s, a few reviews of microbeam in detail had been published [3, 4, 5], but there had been a silent period for microbeam applications. Until 1990s, in the field of radiation biology, a resurgence of interests in use of single-particle microbeam has experienced in order to study a number of newly discovered important radiobiological effects which cannot be done by conventional broad-filed source.

Deterministic and stochastic effects associated with high dose and high dose rate have been well discovered and quantified based on large amount of available data like Japanese atomic bomb survivor Life Span Study (LSS). The risk due to environmental and occupational exposure to Low dose and low dose rate radiation , there are many unknowns for the stochastic effects due to very limited data. In contrast to deterministic effects, for stochastic effects, scientific community generally assume there is a positive linear relationship at low dose between dose and excess cancer risk extrapolated from high dose region, that is linear non-threshold (LNT) theory [6]. The difficulties on detecting statistic significant increase in radiation induced cancer from large background of population make the mean of epidemiological study at low dose region lacking of statistical confidences. Recently, different opinions against LNT have raising from new finds such as genomic instability, bystander effect, hypersensitivity and adaptive response etc. These radiobiological effects may suggest a more complex mode to describe the dose-response relation at low dose region. For example, generally speaking, bystander effects show a irradiated cell can send out a signal and trigger response in neighboring unirradiated cells which may result in genetic damage or instability and may be lethal to unirradiated cells, but some favorable bystander

effects on cells include enhanced cell differentiation, increased cell proliferation and a radioprotective adaptive response [7]. To reveal the full picture of the dose-response curve, experimental investigation of biological responses at low dose and low dose rate region is critically important.

At low dose, individual cells only rarely experience traversals by ionizing particles [8]. The conventional sources are not capable for delivering exactly one particle to one cell due to randomness from Poisson distribution. Radiobiologists had been seeking for a suitable *in vitro* experiment to simulate the exposure that occur *in vivo* and they found the microbeam. With the capability of highly localized spatial irradiation on selective part of cells, it allows directly investigation the intercellular and intracellular communication for bystander effects study [9]. Microbeam facilities allow precise irradiation to a certain type and numbers of cells which can establish a direct correlation between radiation-induced damage, number and energies of particle and dose rate to a defined group of cells or a particular cell site [8]. By coupling microbeams with technological advances in particle delivery, beam focusing, digital imaging processing and computer control, a new generation of modern single-particle microbeam had been operational or under development by different groups around the world in the past decade [10, 11, 12, 9].

To achieve the goal of single-ion irradiation, there are some requirements have to be fulfilled: (1) micro-meter or sub-micrometer size beam spot with appropriate energy particles, (2) extracted beam into air to work with living cells, (3) a cell visualization/observation system based on a microscope equipped with a CCD camera, (4) a micropositioning system to locate the cells under the microscope and in the beam, (5) a high efficiency particle detector to count the number of ions hitting

and/or traversing the cell and to trigger the mean of switching off the beam once the desired number of ions has been delivered [8]. The designs of microbeam facilities in institutions around the world have been adopting different approaches to meet these criteria. Table 1.1 summarized the features of operational microbeam facilities around the world.

### 1.1.2 Beamline Formation and Vacuum Window

The beamline configuration can be categorized into vertical and horizontal. The vertical beamline means the ions coming to the irradiation room from above or below, which makes the cells observation becoming easier. The facilities with horizontal beamline configuration usually takes the advantage of the existing accelerator beamlines. MeV-level protons and alpha particles are the common source in charge particles microbeam facility while some faculties can produce heavy ions. In order to make the beam size to micrometer or sub-micrometer scale, one approaches is collimator and another is magnetically or electrolytically focusing. The way of mechanical collimation is straightforward and cost-friendly applied by many facilities such as Radiological Research Accelerator Facility (RARAF) Columbia University I (New York, USA) and Gray Cancer Institute (GCI, London, UK). RARAF Columbia University I operated from 1994 for biological experiments and decommissioned on 2004. It designed a double apertures final collimator system containing two laser-drilled stainless steel foils with a  $5\ \mu\text{m}$  (limiting aperture) and a  $6\ \mu\text{m}$  (anti-scattering aperture to chop off beam penumbra due to single split diffraction) diameter hole respectively separated by a  $300\text{-}\mu\text{m}$  spacer mounted in the shallow recess of a snout projecting from the end of the beam line and positioned by two orthogonal micrometers, a  $3.7\ \mu\text{m}$  radius

beam core with 92 % of ions can be achieved [9]. GCI used either a 'V'-groove or a thick-walled glass capillary to achieve up to 2  $\mu\text{m}$  spatial resolution [13]. Compared to collimation, focusing can provide narrower beam size and higher spatial resolution without sacrificing beam current, but it is also relatively complicated since need to consider focused system installation issue and cost. The focusing of beam usually requires many components working together including electrostatic deflection plates, slits and quadrupole doublet magnets. Physikalisch-Technische Bundesanstalt (PTB, Brunswick, Germany) achieved 2  $\mu\text{m}$  beam width (FWHM) [14]. Superconducting Nanoscope for Applied Nuclear (Kern-) Physics Experiments (SNAKE, Munich, Germany) was able to adapt irradiation accuracy of 0.91  $\mu\text{m}$  (FWHM) when irradiating with 100 MeV  $^{16}\text{O}$  ions [15]. RARAF Columbia University II changed the collimated beam into focusing beam by a compound lens consisting of four electrostatic quadrupoles with a Russian quadruplet configuration [16] and achieved 0.8  $\mu\text{m}$  beam spot size in air for 6 MeV alpha particles [17]. The performance of living cells irradiation by charge particles requires extracting ions from the accelerator beamline which means going out the vacuum. Vacuum window as the last part that one ion exiting the beamline can cause scattering reducing the beam spatial resolution. In order to minimize the influence of the extraction window, vacuum-tight windows consisting thin film of polymers (mylar, kapton or polypropylene) or  $\text{Si}_3\text{N}_4$  membranes [8].

### 1.1.3 Cell Recognition and Observation

Microscopes are essential for the study of radiobiology to identify and recognize the change in irradiated cells. Cell staining and fluorescence microscopy is a method

that label the specific molecules in the irradiated target by dyes and these stained cells can be observed by a fluorescent microscope coupled to a CCD imaging system. A fluorescent microscope uses UV light or laser as the illuminator to expose the target and receives the excited fluorescence from the target to construct images, so it usually requires a light-proof cage to avoid the disruption from environmental light. Appropriate software can log cells' positions into a coordinate which is recalled to localize cells in the beam by translation stages with submicrometric precision. An on-line automatic cell recognition can be performed. This method was applied by Columbia University [9], GCI [13], GSI (Darmstadt, Germany) [18], CENBG (Bordeaux, France) [19] and Japan Atomic Energy Research Institute (JAERI, Takasaki, Japan) [20]. Instead of a fluorescent microscope, many facilities used phase contrast optical microscopes such as INFN-Laboratori Nazionali di Legnaro (INFN-LNL, Padova, Italy) [21], PTB [14] and SNAKE [15]. Since for phase contrast optical microscopes, regular light illuminator is used and imaging analysis is based on phase contrast grayscale images, cell staining and UV light can be avoided. However, the disadvantage is that only semi-automatic cell recognition procedures can be implied.

### **1.1.4 Particle Detection**

#### **Pre-cell Configuration**

A detector that can measure the number of ions hitting the cells is essential to a charged particle microbeam facility. The charged particle detector can be performed either before or after the cell holder. Pre-cell configuration refers to placing a detector between the extraction window and the cell holder. In this configuration, it is able to count the number of upcoming ions without constraints imposed on thick tissues that

ions cannot penetrate and target need immersion microscopy or microfluidic device involved. When a charge particle traverses through a detector, it will deposit energy into the medium and perform scattering within the detector which means energy lose and spatial accuracy degradation. Hence, only a thin transmission-type detector is appropriate in this configuration in order to minimized the influence on beam size and energy lose. A common and successful solution for pre-cell configuration is to use a thin plastic scintillator coupled with a photon multiplier tube (PMT) because thin plastic scintillator is penetrable by ions. Ions interact with the scintillator and generate light which collects by PMT to produce signal. GCI initially chose zinc sulphide doped scintillator due to the highest efficiency of any scintillator but the long decay time made them turned to an 18  $\mu\text{m}$  thick layer of organic plastic scintillator NE102A (BC400 equivalent) where is on the top of a 3  $\mu\text{m}$  thick Mylar window of the collimator [13]. The PMT was mounted on the microscope objective turret right above the cell holder. Once cells' positions are in right place and logged, the PMT can be positioned over the cell dish by rotating the turret and then irradiation process can start. PTB also applied a 10  $\mu\text{m}$  BC400 scintillator-PMT method as the pre-cell detector system for ions counting [14]. Other options like gas detector and semiconductor detector can also achieve the objective of counting but need to overcome the challenge on how to build it super thin. A low pressure proportional counter (10 mbar, isobutane) fitted in a 3.5 mm chamber with  $\text{Si}_3\text{N}_4$  entrance/exit windows has been designed at CENBG [19]. Lund Nuclear Microprobe (NMP) facility at Lund University (Lund, Sweden) used a custom-built ultra-thin n-type silicon detector in the thickness range from 8 to 10  $\mu\text{m}$  and its detection efficiency is 99% for alpha particles and 2 MeV proton [22]. RARAF Columbia university developed

a super-thin Schottky barrier (the rectifying junction at the interface of a metal and a semiconductor) diode by depositing aluminum and gold electrodes onto silicon as a novel pre-cell detector [23].

A special pre-cell or may be categorized as another configuration was purposed by researchers at GSI: use an indirect method to detect secondary electron cloud released from the target after ion impact rather than a transmission-type detector to avoid destruction of the quality of microfocus. A channel-electron-multiplier was mounted closed to the extraction window to detect secondary electrons produced by ions crossing the window. To increase the hit detection efficiency by increasing the secondary electron yield, surface coatings of CsI-layer showed better secondary electron yield spectra than undoped/B-doped chemical vapor deposited (CVD) diamond coating [24].

### **Post-cell Configuration**

Post-cell configuration means the particle detector is placed behind the cells target. The advantage of this configuration is no effect on beam scattering by the detector and relevantly easier to apply with existing detectors, but it requires that ion energy must be high enough to pass through the cell sample in this case. The choices of detector include scintillator-PMT, silicon surface barrier detector and gas detector. At SNAKE, a 17  $\mu\text{m}$  thick scintillator on top of a small PMT was placed in the turret of the optical microscope enclosed by 5  $\mu\text{m}$  aluminum foil and 0.9  $\mu\text{m}$  aluminised Mylar foil to protect the assembly against ambient light [15]. JAERI also applied a scintillator coupled with a PMT mounted on the microscope turret [20]. A silicon surface barrier detector was placed behind the cell chamber at INFN-LNL [21]. Lund

Single Ion Hit Facility used silicon surface barrier detector for post cell detection [25]. A double-sided silicon strip detector with 64 sector strips and 32 ring strips given more than 2000 detector cells, each with characteristics comparable with a standard surface barrier detector, was developed in Lund university [26] and it could be used for the microbeam application. At RARAF Columbia university, the detector they used was a pulsed ion counter filled with P10 gas (90% argon + 10% methane) mounted on the microscope objective [9].

### **1.1.5 Conclusion**

Modern charge particle microbeams are able to deliver single-ion irradiation which provides an extraordinary way to experimental determine the low dose and low dose rate radiation effect. Various microbeam facilities around the world had successfully operated and performed experiments by adapted different approaches in beamline formation, vacuum window, cell observation, and ion detection.

Table 1.1: Features of selected charged participle microbeam facilities

<b>Facility</b>	<b>Beamline formation</b>	<b>Cell Observation</b>	<b>Detection Configura- tion</b>	<b>Detector</b>
RARAF I/II, New York, USA [9, 17, 23]	Vertical, Collima- tion/Focusing, 6 MeV $^4\text{He}^{2+}$	Fluorescent microscope with cell staining	pre-cell <hr/> post-cell	Schottky barrier detector <hr/> Pulsed ion counter filled with P10 gas
GCI, London, UK [13]	Vertical, Collimation, 4-8 MeV $^1\text{H}^+ / ^4\text{He}^{2+}$	Fluorescent microscope with cell staining	pre-cell	Plastic scintillator (18 $\mu\text{m}$ thick NE102A)
PTB, Brunschwig, Germany [14]	Vertical, Focusing, 1-20 MeV $^1\text{H}^+ / 28$ MeV $^4\text{He}^{2+}$	Phase contrast optical microscopes	pre-cell	Plastic scintillator (10 $\mu\text{m}$ thick BC400)

*Continued on the next page*

*Continued from previous page*

<b>Facility</b>	<b>Beamline formation</b>	<b>Cell Observation</b>	<b>Detection Configuration</b>	<b>Detector</b>
GSI,Darmstadt, Germany [18, 24]	Vertical, Focusing, 1.4-11.4 MeV/u from ${}^4\text{He}^{2+}$ to U-ions	Phase contrast optical microscopes	pre-cell/detecting secondary electron	CsI layer+channel-electron-multiplier
CENBG, Bordeaux, France [19]	Horizontal, Focusing, 1-3.5 MeV ${}^1\text{H}^+ / {}^4\text{He}^{2+}$	Fluorescent microscope with cell staining	pre-cell	low pressure proportional counter filled with isobutane
JAERI, Takasaki, Japan [20]	Vertical, Focusing, 13 MeV/u ${}^{20}\text{Ne}$ 11.5 MeV/u ${}^{40}\text{Ar}$	Fluorescent microscope with cell staining	post-cell	Plastic scintillator
SNEAK, Munich, Germany[15]	Horizontal, Focusing, 20-200 MeV from ${}^1\text{H}^+$ to heavy ions	Phase contrast optical microscopes	post-cell	Plastic scintillator (17 $\mu\text{m}$ thick BC400)

*Continued on the next page*

*Continued from previous page*

<b>Facility</b>	<b>Beamline formation</b>	<b>Cell Observation</b>	<b>Detection Configura- tion</b>	<b>Detector</b>
INFN-LNL, Padova, Italy [21]	Horizontal, Focusing, 1-14 MeV $^1\text{H}^+ / ^4\text{He}^{2+}$	Phase contrast optical microscopes	post-cell	silicon surface barrier detector
Lund NMP Lund University, Lund, Sweden [22, 26]	Horizontal, Focusing, 1-3 MeV $^1\text{H}^+$	Phase contrast optical microscopes	pre-cell   post-cell	Ultra-thin n-type silicon detector Double sided silicon strip detector (under development)

## 1.2 McMaster University Microbeam Facility

The first-generation collimation microbeam, RARAF Columbia University I, was decommissioned in 2004 and a new focusing microbeam system was built referred as RARAF Columbia University II. The decommissioned collimator assembly (described in section 1.1.2) of RARAF Columbia University I was then relocated to McMaster

Accelerator Laboratory (McMaster University, Hamilton, Ontario, Canada) for microbeam development [27]. A 3 MV KN Van de Graaff accelerator works as the ion source which can produce mono-energetic proton and alpha particles up to 6 MeV. The beam initially travels through a horizontal trajectory and then is bent 90° upward by an analyzing magnet into the irradiation room forming a vertical beamline. The end station contains a Prior Scientific ProScan II X-Y stage and a Mad City Labs (MCL) nao-positioning XYZ stage for precise target localization and alignment. Cell recognition and observation is processed by a multipurpose microscope (Nikon AZ100) which can work as epi-fluorescent or phase contrast optical microscope by changing the illuminator and attachments. Figure 1.1 demonstrates the overall layout. McMaster microbeam facility is under development at this stage.

### 1.3 Motivation and Objective

As an essential requirement for any microbeam facility, a charged particle detection system need to be developed for McMaster microbeam facility in order to count the number of incoming ion. The 3 MV KN Van de Graaff accelerator at Master microbeam facility can produce maximum 6 MeV double charged light ions. Post-cell configuration is not feasible since 4-6 MeV ions is not or barely enough to pass through the biological sample. For pre-cell configuration, thin plastic scintillator is widely applied by many facilities due to its excellent transmission. However, for very thin plastic scintillator, the light it emitted after interacting with ions is very weak and usually close to the lower detection limit of the PMT. In order to keep PMT signal noise low, unwanted source of light, electrical noise and dark current must to be eliminated or minimized. To eliminate ambient light, irradiation room is usually

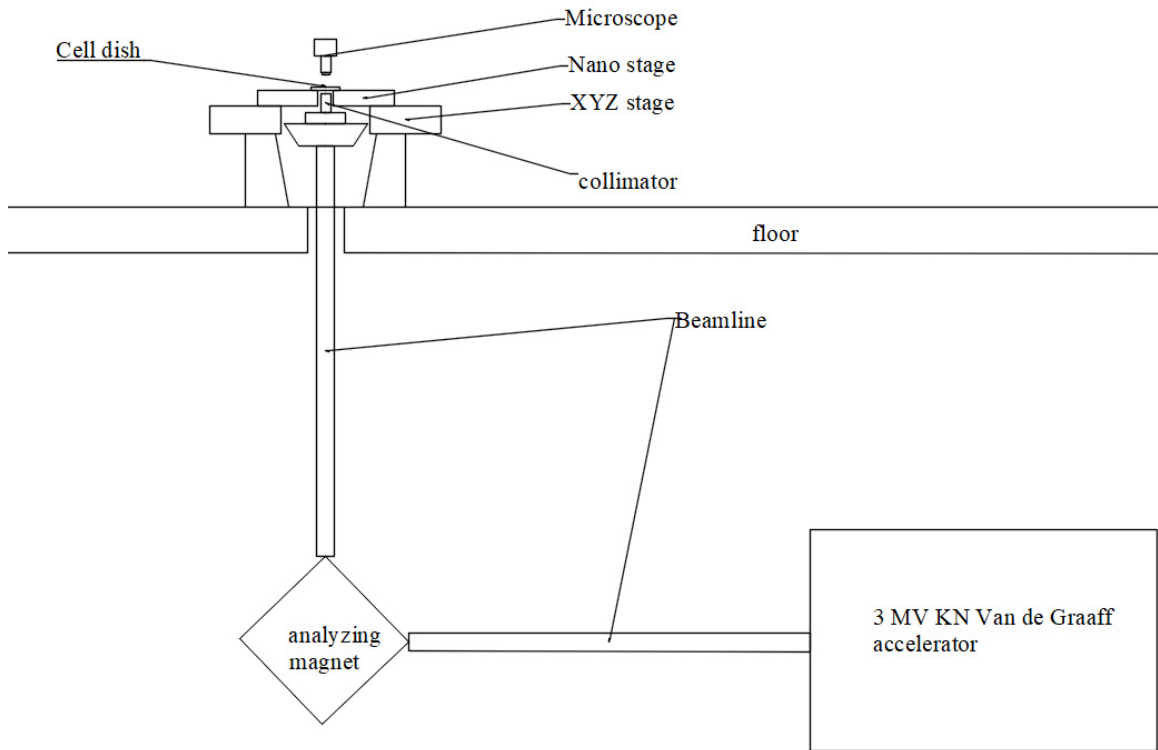


Figure 1.1: Schematic drawing of the overall layout of McMaster microbeam facility. No distance or sizes are to scale and is for demonstrative purpose only

enclosed in a light-proof cage and no optical observation through the microscope during the irradiation. Interconnection of different systems needs to be strictly adhesive to reduce electrical noise. Super efficient PMT with low dark current is required to work on very low illumination conditions, but the limitation on PMT installation restricts its performance since a PMT is usually mounted on the microscope turret and no extra place for extra cooling. A silicon Schottky diode is light sensitive as well required special light gathering. Low pressure gas detector is very complicated in engineering integration with the existing end station. We are looking for a novel detector to overcome these issues of common ion detection systems and to provide

a robust and reliable counting performance at McMaster microbeam facility. The development of a ion counter for microbeam had been previously studied by Urlich [28] and Tong [29]. Urlich designed and constructed a silicon Schottky diode for proton counting and Tong purposed and developed a thin single crystal chemical vapor deposited (ScCVD) diamond transmission-type alpha particle counter.

Diamond has uniquely stable physical and chemical property and has been increasingly interested as a wide band gap semiconducting material triggered by chemical vapor deposition, a revolutionary diamond synthesis technique. CVD diamond detector had been fabricated and contributed in many physics experiments like as beam loss monitors in Large Hadron Collider (LHC). ScCVD diamond as a unique semiconductor detector has excellent mechanical propriety, wide band-gap, great radiation hardness, high breakdown voltage, fast charge carrier mobility and the best thermal conductivity at room temperature. A thin ScCVD membrane can be used as a detector and also as an extraction window [30] to further reduce the beam scattering compared to a detector placed after the extraction window. Tong compared energy lose and cumulative lateral hitting probability distribution within  $10\ \mu\text{m}$  for silicon, diamond and proportional gas-filled detector via Monte Carlo simulations, the result indicated ScCVD diamond has comparable energy loss with silicon and smallest scattering to the beam size [29]. The fabrication process including plasma etching, sputtering, electric contact and wiring had been discovered. Spectra of  $250\ \mu\text{m}$  and  $50\ \mu\text{m}$  thick ScCVD diamond had been collected and proved the feasibility of diamond as a transmission-type alpha counter in her work [29].

The objectives of this work are to continued on development of ScCVD diamond detector and to build an ultra-thin ( $< 10\ \mu\text{m}$ ) ScCVD diamond detector which can

be used as both pre-cell detector and extraction window at McMaster microbeam facility. By constructing an  $\Delta E$ -E detectors system, the transmission property of the ultra-thin diamond detector can be verified. In this work, fundamental properties of diamond and principles of diamond as a solid state detector for charge particle radiation will be studied. The improvements in fabrication will be described. Experimental results of the ultra-thin diamond detector and  $\Delta E$ -E detectors system will be presented and discussed.

## Chapter 2

# Chemical Vapor Deposited Diamond

Diamond, as a kind of shining precious jewelry, is the symbol of nobility and elegance. It is also well known as a unique indestructible material that has supreme hardness, singular strength, high thermal conductivity, chemical inertness, excellent visible/infrared light and X-ray transparency. Although the great value of diamond as an industrial material had been recognized since antiquity, the rareness and consequently expensive prices limited the application of diamond until recently development of chemical vapor deposition (CVD) technique allowing industrial scale production of high quality synthetic diamonds.

## 2.1 Physical Properties of Diamond

### 2.1.1 Diamond Lattice

Natural diamond is a solid form of carbon containing natural abundance 98.9%  $^{12}\text{C}$  and 1.1%  $^{13}\text{C}$ . The electron configuration of carbon in the ground state is  $1s^2 2s^2 2p^2$ . The hybridization of  $sp^3$  (tetrahedral) orbital state accounts for the valence state of a carbon atom with four  $2sp^3$  orbitals. These orbitals in each carbon atom are bonded to the orbitals of four other carbon atoms by strong covalent bonds to form a regular tetrahedron (triangular prisms) [31]. The tetrahedron of diamond makes a covalent crystalline structure, most commonly in cubic. Diamond has a face-centered cubic (FCC) lattice structure with two carbon atoms at each Bravais lattice point. The cube edge length in pure diamond measured by X-ray diffraction in room temperature is 0.357 nm [32]. Two populated C atoms are separated by 0.154 nm which is smaller compared to other semiconductor material like silicon (0.234 nm). Each diamond unit cell contains eight carbon atoms. The structure of diamond is shown in Figure 2.1. Diamond has the highest atom density of any material with a molar density of 0.293 g-atom/ $\text{cm}^3$  which is why diamond is the hardest and least compressible substance in Earth. The density of diamond is  $3.52 \text{ g/cm}^3$ .

### 2.1.2 Band Structure and Band Gap

In solid state physics, the idea of energy bands, separated by band gaps, had been introduced to characterize the electronic behavior in solids. Diamond's properties are closely related to its band structure.

The  $s$  and  $p$  electrons are considered as the valence electrons. When electrons

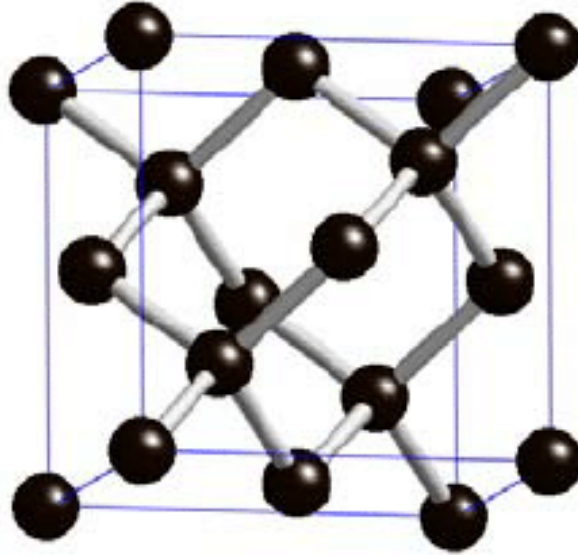


Figure 2.1: Schematics of the diamond cubic structure, showing the tetrahedral orientation of each C atom [33]

are accommodated in the bonding orbital, they have opposite spins to obey the Pauli Exclusion Principle, and the bonding and antibonding molecular orbitals are formed as two atoms approach each other while the energy levels are a function of interatomic separation [34]. The splitting and overlap of  $s$  and  $p$  bonding/antibonding curve form a quasi-continuum of energy states. This quasi-continuum is called an energy band. For metal,  $s$  and  $p$  bands do not mix when atoms approach each other (Figure 2.2(a)) [35]. The energy band is half-filled with electrons and one is half empty. Thus, when voltage is applied, valence electrons in lower state can go into a slightly higher energy state very easily because there are plenty of unoccupied states available at slightly higher energies. For some other material like silicon, the lower  $sp^3$  band is fully occupied by all four valence electrons and completely unoccupied in the upper band due to  $sp^3$  hybridization (Figure 2.2(b)). The highest occupied band and the the lowest unoccupied band are valence band (VB) and conduction band (CB). There

is a forbidden energy region without any energy state which is called band gap. The electrons must gain sufficient energy larger than the band gap to be conducting, otherwise it is insulating.

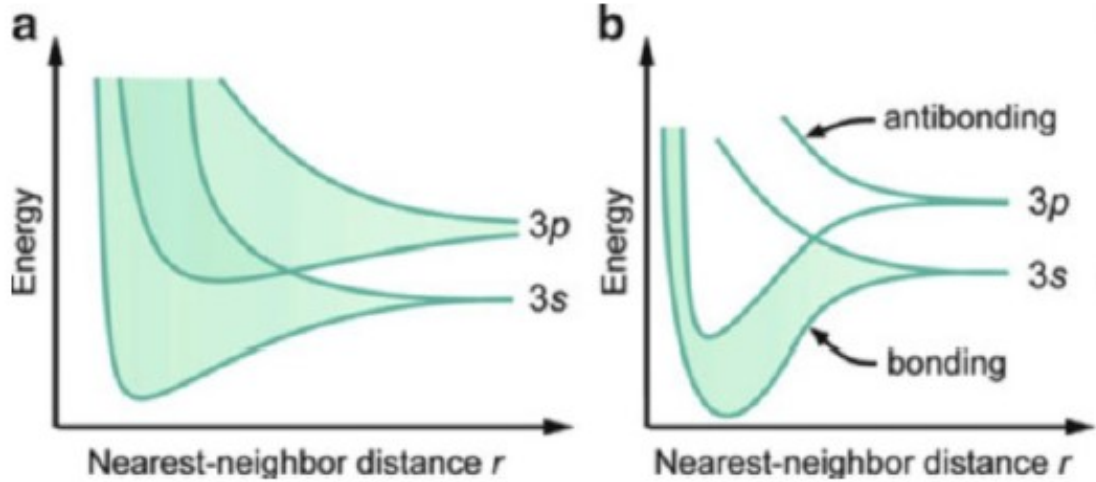


Figure 2.2: Electronic energy distribution for a crystal as a function of the interatomic nearest-neighbor distance  $r$ . (a) Overlap of  $s$  and  $p$  bands in main-group metals. (b)  $sp^3$  hybridization in covalent tetravalent elements [35]

To find the allowed energy states of electrons in the solid, it means the quantum mechanical eigenstates governed by the solution of wave function. The stationary Schrödinger equation for the electronic states of one electron moving in an effective potential  $U(r)$ , given by all the ions and all the other electrons

$$-\frac{\hbar^2 \nabla^2}{2m_e} \psi(r) + U(r) \psi(r) = E \psi(r) \quad (2.1.1)$$

Due to symmetry of the lattice, the effect potential  $U(r)$  is lattice-periodic

$$U(r) = U(r + R) \quad (2.1.2)$$

where  $\mathbf{R}$  is any vector of Bravais lattice.

The Bloch's theorem indicates the complete set of eigenstates of Equation 2.1.1 can be written in the form

$$\psi_{\mathbf{k}}(\mathbf{r}) = e^{i\mathbf{k}\cdot\mathbf{r}} u_{\mathbf{k}}(\mathbf{r}) \quad (2.1.3)$$

$\mathbf{k}$  in  $u_{\mathbf{k}}(\mathbf{r})$  is the wave vector and it is also referred as Bloch vector. The corresponding energies  $E(\mathbf{k})$  are functions in the Bloch vector  $\mathbf{k}$  representing the energy for bands.

Energy dispersion curves in Figure 2.3(a) which demonstrates the band structure of diamond as a function of Bloch vector  $\mathbf{k}$  was calculated from *Ab Initio* using discrete variational method [36]. The Bloch vector in the energy dispersion diagram is usually denoted by points in the first Brillouin zone (Figure 2.3(b)) which is the Wigner–Seitz cell of the reciprocal lattice.  $\Gamma$  is the center of the zone in a cubic lattices,  $X$  is the intersection of the Brillouin zone surface with any of the main axes. Those points also correspond to Bloch-vector  $\mathbf{k}$ , ranging from  $-\frac{\pi}{d}$  to  $\frac{\pi}{d}$ . For example,  $\Gamma$  denotes  $\mathbf{k}=0$ . Two dash lines in Fig 2.3(a) indicate VB and CB. Since only the valance band maximum (VBM) of the diamond locate at  $\Gamma$  and the conduction band minimum (CBM) is found at between  $\Gamma$  and  $X$ , the gap here is an indirect band gap equal to 5.47 eV at 300 K. Diamond, as a indirect band gap material, it has six conduction band minimum (valleys) at symmetrically equivalent directions in the Brillouin zone along the [100] direction.

Diamond's wide band gap is much larger than other group-IV element like silicon and germanium which has band gaps of 1.12 eV and 0.66 eV respectively. The classic definition of a semiconductor is the material with band gaps below 3 eV [34] or 5 eV [37]. Therefore, diamond is typically classified as an insulator but it is also considered as a wide-bandgap semiconductor if define a semiconductor as electrons in

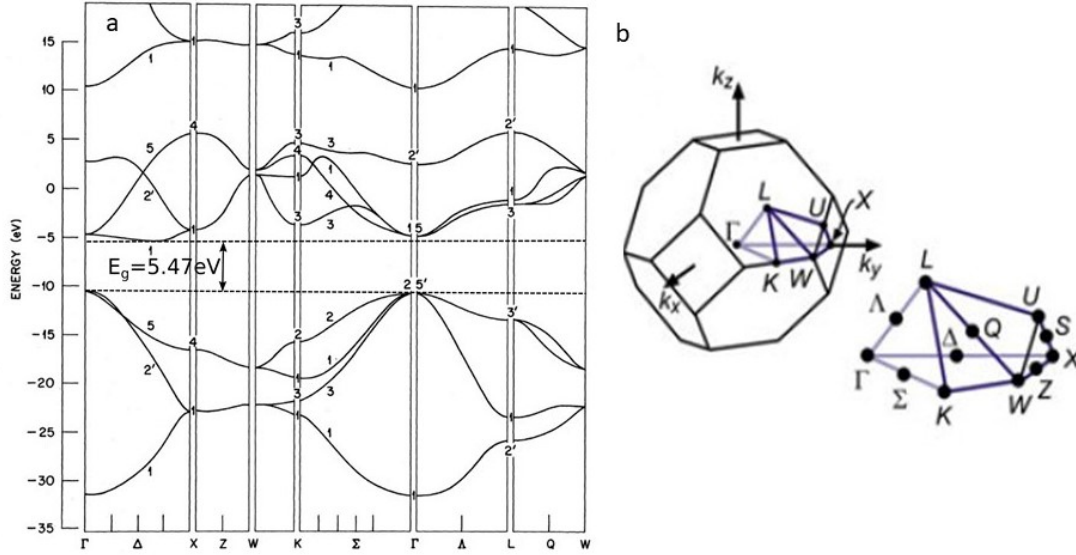


Figure 2.3: (a) The band structure of diamond [36]. Dashed lines mark the 5.47 eV band gap between valance band maximum (VBM) and conduction band minimum (CBM). (b) First Brillouin zone for the FCC lattice [35]

the conduction band and holes in the valence band are free to move under the influence of an applied force [38]. The wide band gap of diamond promises visible light blind and insensitivity to temperature. These features are particularly considered as the advantage for diamond-base detector applied on microbeam end station over other choices. Unlike in the case of plastic scintillator, light gathering system or light-proof cage is not required for the operation of diamond detector and the real-time cellular responses can be observed via the optical microscope.

### 2.1.3 Lattice Vibration and Thermal Conductivity

The atoms in a crystal perform vibration about their equilibrium position even at lowest temperatures. Starting from the classic description of wave propagation as a

simple harmonic oscillator, consider atoms at the lattice site are connected to their neighbors with springs of a force constant  $\gamma$ , the motion equation for an atom  $n$  is

$$M \frac{\partial^2 u_n}{\partial t^2} = -\gamma(u_n - u_{n-1}) + \gamma(u_{n+1} - u_n) \quad (2.1.4)$$

where  $M$  is the mass of the atom,  $u_n$  is the displacement of the  $n$ th atom in the atom chain. This equation can be solved if define  $u_n$  as a kind of wave

$$u_n(t) = u e^{i(kan - \omega t)} \quad (2.1.5)$$

where  $k=2\pi/\lambda$  is the wave vector,  $u$  is the amplitude of the oscillation. Substitute this into equation 2.1.4

$$M\omega^2 e^{i(kan - \omega t)} = 2\gamma(1 - \cos(ka)) e^{i(kan - \omega t)} \quad (2.1.6)$$

and this has a solution if  $\omega = \omega(k)$  that

$$\omega(k) = \sqrt{\frac{2\gamma(1 - \cos(ka))}{M}} = 2\sqrt{\frac{\gamma}{M}} \left| \sin\left(\frac{ka}{2}\right) \right| \quad (2.1.7)$$

The particular solution of the motion with  $\omega(k)$  is called a normal mode of the chain. Equation 2.1.7 connects the frequency or energy to wave vectors which is called dispersion relations. There are two solutions in the first Brillouin zone for the vibration of a chain with two or more atoms, one is the acoustic branch that goes to zero for small  $k$  corresponding to sound wave, another is the optical branch which has a finite  $\omega$  at  $k=0$  relating to the oscillating electrical field of electromagnetic wave.

The quantization of normal mode gives the quantized energy levels  $l=0,1,2,3,\dots$

$$E_l(k) = (l + \frac{1}{2})\hbar\omega(k) \quad (2.1.8)$$

where  $k = \frac{2\pi m}{aN}$  for a chain of  $N$  atoms with a spacing of  $a$  and it plays the role of wave vector and quantum number as well. The normal modes can be excited in discrete energy quanta and this excitation is called phonons, a kind of quasiparticle in analogy to photons. Equation 2.1.7 is called phonon dispersion relation.

Phonons and electrons are responsible for the heat transport in a crystal. In diamond, there is almost no free electrons due to the wide band gap. As the result, only phonons dominate the heat transport. The lattice thermal conductivity can be calculated from

$$\kappa = \frac{1}{3}c\lambda_p v_p \quad (2.1.9)$$

where  $c$  is the heat capacity,  $\lambda_p$  is the mean free path of the phonons, and  $v_p$  is the phonon speed. Defect scattering and phonon scattering effect both  $\kappa$  and  $\lambda_p$  at low and high temperature respectively.

Diamond has nearly perfect crystal so that defect scattering is less important. Carbon atoms in diamond form very strong covalent bonds, so it requires large amount of energy to vibrate the lattices and it results in extremely high vibration frequency and corresponding Debye temperatures. Thus, phonon-phonon scattering only dominating at very high temperatures. Overall, the diamond has the highest thermal conductivity at room temperatures  $\kappa=2200 \text{ Wm}^{-1}\text{K}^{-1}$  of all known materials [39]. The high thermal conductivity allows a diamond detector operating at high temperature environment without external cooling system.

### 2.1.4 Transport Properties of Charge Carriers

The transport properties of charge carriers are a formidably complicated problem in solid state physics. Due to the limit of scope, only some basic but important concepts are going to be briefly introduced.

#### Bloch Electron and Hole

At nonzero temperature, some electrons in the VB can be elevated across the band gap when they gain sufficient thermal energy. An excited electron leave an empty state in the bonding and the electron surrounding the empty state can move on opposite direction of the electrical field to fill in the missing state. In other words, the empty state moves in the opposite direction of the electron since new empty state is simultaneously created as electron fills the vacancy. Instead of considering the complicated motion of electrons, one can describe the conduction in terms of the moving missing electron or so-called hole [34].

A quasi-classical description of electrical conduction treats the movement of a localized electron as a wave packet (Bloch wave) traveling with a group velocity  $v_g$  that

$$v_g = \frac{1}{\hbar} \frac{dE(k)}{dk} \quad (2.1.10)$$

where  $E(k)$  is the energy of electron depending on its wave vector  $k$ .

Consider an electric field  $\varepsilon$  is applied, an electron with a velocity  $v_g$  can increase its kinetic energy after a short time by

$$dE = -e\varepsilon v_g dt \quad (2.1.11)$$

In addition

$$\frac{dE}{dt} = \frac{dE}{dk} \frac{dk}{dt} \quad (2.1.12)$$

combine this equation 2.1.10

$$\hbar \frac{dk}{dt} = -e\varepsilon \quad (2.1.13)$$

This means that an electric field causes the electron to change the wave vector in a rate proportional to the field strength.

Consider the acceleration of an electron initially traveling with  $v_g$

$$a = \frac{v_g}{dt} = \frac{1}{\hbar} \frac{1}{dt} \frac{dE(k)}{dk} = \frac{1}{\hbar} \frac{\partial^2 E(k)}{\partial k^2} \frac{dk}{dt} \quad (2.1.14)$$

substitute equation 2.1.13 for  $\frac{dk}{dt}$

$$a = -\frac{1}{\hbar^2} \frac{\partial^2 E(k)}{\partial k^2} e\varepsilon \quad (2.1.15)$$

This looks like the classical equation of motion in form of  $\frac{dv}{dt} = -\frac{e\varepsilon}{m_0}$ . If define a so-called effective mass  $m^*$

$$m^* = \hbar^2 \frac{dk^2}{d^2 E(k)} \quad (2.1.16)$$

The effective mass of electron and hole may be smaller or larger than the rest mass depending on the curvature of  $E(k)$  it located which is determined by the actual lattice potential. The electron (described as Bloch electron to distinguish it from an electron in vacuum) and hole with effective mass is free to move when apply electric fields to a semiconductor, which contribute to the electrical conductivity in the solid

and therefore called charge carriers of the current.

## Scattering

when Bloch electrons and holes travel through a crystal, they interact with lattice imperfection such as phonons, impurities and crystal defects which is described in term of scattering. The scattering of carriers acts as a kind of friction that rapidly relaxes the increase of momentum and energy and limits the mobility of the carriers [40].

The carrier scattering can be described by the Boltzmann equation in the form of

$$\frac{\partial f}{\partial t} - \frac{e}{\hbar} \varepsilon \frac{\partial f}{\partial k} + \frac{1}{\hbar} \frac{\partial E(k)}{\partial k} \frac{\partial f}{\partial r} = \left( \frac{\partial f}{\partial t} \right)_{coll} \quad (2.1.17)$$

where  $\varepsilon$  is the electric field,  $f(k,r,t)$  is the Boltzmann distribution function of charge carriers, index *coll* indicates the collision an this collision term describes the net number of electrons forced into the volume element by collision in time interval  $dt$  [41]. A simplified approach to solve equation 2.1.17 is introduced called relaxation-time approximation, in which it assumes that the rate of collision term bring the system back to unperturbed state is linear

$$\left( \frac{\partial f}{\partial t} \right)_{coll} = -\frac{f - f_0}{\tau_m} \quad (2.1.18)$$

where  $f_0$  is the thermal equilibrium distribution function,  $f$  the actual nonequilibrium distribution function due to external disturbance and  $\tau_m$  is the momentum relaxation time which means the average time between two collisions. The total relaxation time contributed from several independent scattering mechanisms can be written in the

equation below, followed Mathiessen's rule

$$\tau^{-1} = \sum_i \tau_i^{-1} \quad (2.1.19)$$

The total scattering is contributed by phonon scattering including acoustic phonon and optical phonon, intervalley scattering, ionized impurity scattering, neutral impurity scattering, dislocations, and surface and grain boundaries. More details can be found in Isberg's review [40].

### Charge Carriers Mobility and Drift Velocity

Charge carriers tend to be more mobile when they experience less scattering. A quantity of mobility is defined as

$$\mu = \frac{q}{m^*} \bar{\tau} \quad (2.1.20)$$

where  $q$  is particle charge,  $\bar{\tau}$  is the mean relaxation time between scattering events. The mobility is negative to electron and positive to hole.  $\mu$  is also referred as drift mobility when charge carriers in an electric field  $\varepsilon$  has a drift velocity

$$v_d = \mu\varepsilon \quad (2.1.21)$$

The anisotropic change of drift velocity in diamond with respect to crystallographic direction is expected [42]. In the high electric field, the charge carriers are heated and no longer in thermal equilibrium with the lattices temperature, which causes more scattering and consequently decreases in mobility. The drift velocity becomes

saturated at sufficiently high field.

The drift mobility is temperature dependent relating to phonon scattering. The mobility of diamond shows a roughly  $T^{-1.5}$  dependency relating to acoustic phonon scattering at temperature below 400 K and drop exponentially with increasing temperature for  $T < 600$  K since optical phonons increase exponentially for temperatures below approximately 30% of the Debye temperature [40]. For nature diamond, the low-field drift mobility is  $2500 \text{ cm}^2\text{V}^{-1}\text{s}^{-1}$  and  $2100 \text{ cm}^2\text{V}^{-1}\text{s}^{-1}$  at 300 K for electron and hole respectively [42]. Measurements on single crystal CVD diamond reported higher charge carriers drift mobility due to photometrically growth. Isberg *et al* reported mobility 3500 to 4500  $\text{cm}^2\text{V}^{-1}\text{s}^{-1}$  for electrons and 2600 to 3800  $\text{cm}^2\text{V}^{-1}\text{s}^{-1}$  for holes using UV laser excitation measured at 25 °C [43]. The measurements by Promorski *et al* indicated the electron mobility 1300 to 3000  $\text{cm}^2\text{V}^{-1}\text{s}^{-1}$  and hole mobility 2330 to 2400  $\text{cm}^2\text{V}^{-1}\text{s}^{-1}$  by using  $\alpha$ -particle while the saturation velocity for electrons and holes in ScCVD was  $1.9 \times 10^7 \text{ cm/s}$  and  $1.4 \times 10^7 \text{ cm/s}$  at field up to  $3 \times 10^4 \text{ V/cm}$  [44]. The high charge carriers mobility of ScCVD can produce fast signal on radiation detector operation. High saturation velocity helps it to maintain fast signal at high electrical field.

### Electrical Conductivity and Resistivity

The conductivity can be defined using the mobility

$$\sigma = qn\mu \quad (2.1.22)$$

where  $n$  is the carrier concentration. And then resistivity is

$$\rho = \frac{1}{\sigma} = \frac{1}{qn\mu} \quad (2.1.23)$$

The intrinsic resistivity of pure diamond can exceed  $10^{16} \Omega/cm$  as one of best solid electrical insulator. The resistivity is greatly effected by impurities and grain boundaries. For born doping diamond, the resistivity is about  $10^{-3} \Omega/cm$ .

### 2.1.5 Dielectrics

Dielectrics refers to an insulator that can be polarized in electrical field. Although there is no current flow in an insulator with electric field applied, electrical charges shift their equilibrium position which causes dielectric polarization  $P$  given by

$$P = \chi_e \epsilon_o \varepsilon \quad (2.1.24)$$

where  $\varepsilon$  is electric field,  $\chi_e$  is electric susceptibility and  $\epsilon_o$  is vacuum permittivity. Dielectric constant  $\epsilon$  relates to  $\chi_e$  in the form of

$$\chi_e = \epsilon - 1 \quad (2.1.25)$$

$\epsilon$  represents the capacitance of the dielectric insulator. The static dielectric constant of diamond is 5.7 which is lower than other semiconductor materials providing low-noise performance of the associated front-end electronics. The dielectric strength, the voltage that an insulating material can withstand before breakdown occurs, is measured as  $30 \text{ V}/\mu\text{m}$  for a  $6.5 \mu\text{m}$  ScCVD diamond [45].

property	Diamond	Silicon	Germanium
Atomic number	6	14	32
Density [ $gm^{-3}$ ]	3.52	2.32	5.32
Band gap (300K) [eV]	5.47	1.12	0.67
Thermal conductivity [ $Wm^{-1}K^{-1}$ ]	2200	150	60
Electron mobility [ $cm^2V^{-1}s^{-1}$ ]	1450-4500	1500	3900
Hole mobility [ $cm^2V^{-1}s^{-1}$ ]	1800-3500	480	1900
Saturation velocity [cm/s]	$10^7$	$10^7$	$10^6$
Intrinsic resistivity [ $\Omega/cm$ ]	$10^{16}$	$2.3 \times 10^5$	47
Dielectric constant	5.7	11.9	16.2

Table 2.1: Physical properties of selected semiconductors. Data are adapted from [46, 37, 47]

Table 2.1 summaries the physical properties of diamond and the comparison to silicon and germanium.

## 2.2 Basics of Chemical Vapor Deposition

Artificial synthesis of diamond had been a tremendous challenge until the invention of high pressure high temperature (HPHT) method in 1954 in General Electric Company. At almost the same time, a low-pressure gas-phase synthesis technique using pyrolysis of hydrocarbon gases was also developed in the USSR by Eversole of the Union Carbide Corporation [48]. Eversole's work was successfully duplicated on natural diamond substrate by Angus and co-workers who used atomic hydrogen as an etchant for graphite [49]. The early work done by Soviet scientists on chemical vapor deposition (CVD) was not actively followed by the U.S, but Japan. Under the leadership of the National Institute for Research in Inorganic Materials (NIRIM), a breakthrough in CVD growth on non-diamond substrate was made in 1982 which significantly reduce the cost of CVD [50]. In 1980s, the development of fast growth-rate CVD process for polycrystalline diamond and epitaxial growth techniques using microwave plasma enhanced CVD (MWPECVD) were reported by NIRIM [51, 52]. Compared to HPHT, the CVD method allows to produce diamond on large area of substrates with controllable impurities. Nowadays, CVD synthesis techniques has been widely studied and applied by research and industrial bodies to produce varies grades of CVD diamond at relatively low costs, which significantly accelerated the development of diamond-related applications.

The general principle of CVD of diamond is to deposit carbon-containing gases on the substrates to grow a diamond coating layer. The precursors gas as the carbon source can be methane, acetylene, methyl alcohol etc. The basic reaction of CVD involves the decomposition of a hydrocarbon via the activation which can be achieved by thermal method (hot filament) or plasma (DC/RF/Microwave). Other conditions

for well defined growth includes high substrate temperature (typically 700 ) and a carbon containing precursor gas diluted in excess of  $H_2$  [53]. Figure 2.4 describes the CVD process. The nucleation of throughout the substrate surface is the first step of the diamond film formation and it depends on many parameters including gas composition and concentration, choice and pre-treatment of the substrate, pressure and temperature. The nucleation process creates a intermediate layer formed by graphite crystallites and carbon granules on the substrate, then diamond particles grow upon the layer. The growth stage is also influenced by many conditions such as temperature, pressure and precursor gas. There are many review articles on the growth of diamond by CVD in the literature [54, 55, 56, 57].

The polycrystalline CVD diamond (PcCVD) consisting numerous small grains in various orientations. For electronic device and detector, the single crystal (monocrystalline) CVD (ScCVD) diamond is preferred. The homoepitaxial growth of ScCVD diamond requires a monocrystalline diamond substrate, usually used HPHT synthetic single crystal diamond. The quality of the diamond produced is associated with substrate pre-treatment, microwave power and many other factors [58].

## 2.3 CVD Diamond Surface and Contacts

### 2.3.1 Surface Termination

The surface of CVD diamond is always hydrogenated due to exceed amount of hydrogen radicals in the precursor gas on the CVD process. The H-terminated induces the p-type conduction surface with negative electron affinity (-1.3 eV) which means the vacuum level is energetically below the conduction band minimum [60]. The

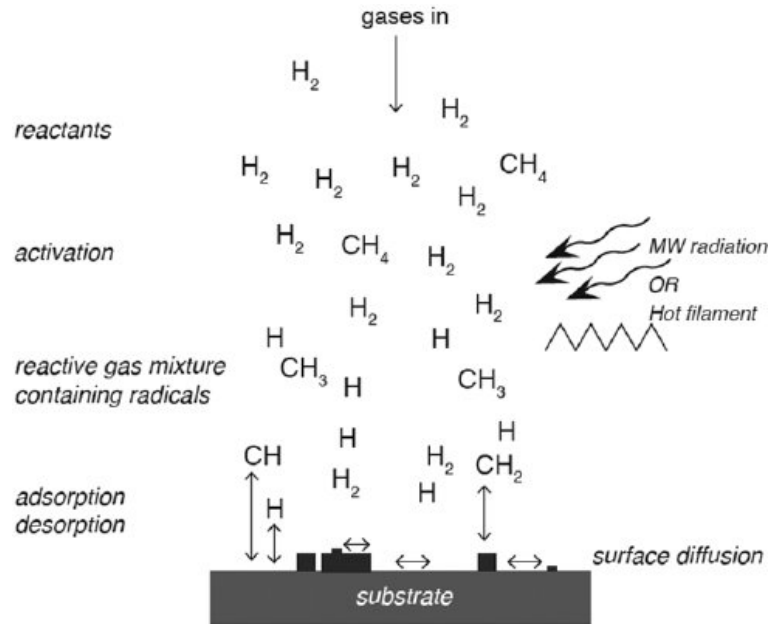


Figure 2.4: Schematic description of the CVD process via activation of MW or heat filament [59]

negative electron affinity provides surface conductivity because the excited electron from conduction band can escape to vacuum easier required less ionization energy. H-terminated surface is generally stable under atmosphere at ambient temperature, but it is chemically active and the surface can be turned into oxygen-terminated by highly oxidizing media or oxygen plasma. O-termination eliminates the surface conductivity appeared in H-terminated surface and the electron affinity becomes positive (1.7 eV).

### 2.3.2 Contacts

Metal contacts are essential to extract charges from the diamond. Depending on the current-voltage characteristics, the contacts can be classified into Ohmic and Schottky contacts. In any solid state material, there is a Fermi level  $E_F$ , the highest

energy state that electrons can occupy at 0 K. When a metal and semiconductor are brought into intimate contact, free carriers will flow from one to another until the Fermi levels equalize in both solids. Due to lower charge density in the semiconductor, the net flow of charge carriers results in re-establishment of electric field at the metal/semiconductor interface and the creation of a potential difference (the Schottky barrier,  $\phi_B$ ) given by

$$\phi_B = \phi_m - \chi \quad (2.3.1)$$

where  $\phi_m$  is the metal work function,  $\chi$  is the electron affinity of the semiconductor. The net flow of carriers also induces a depletion region  $W$  extending into the semiconductor side which causes the bending on semiconductor energy bands as Figure 2.5. The higher Schottky barrier, electrons have less probability to tunneling the potential. The barrier can be lowered sufficiently to allow current to pass unimpeded in one direction under forward bias or raised sufficiently to prevent the passage of current on the other direction (the reverse bias direction) [61]. In this way, the contact is called Schottky, or blocking or rectifying contact which has non-linear and asymmetric current-voltage characteristics. In contrast to Schottky contact, Ohmic contact is defined as one with a negligibly small impedance compared to the series impedance of the bulk of the semiconductor [62]. Although the current-voltage relationship is not really linear in some cases, the transfer of carriers is unimpeded independent on polarity or bias direction. Ohmic contact does not affect the transfer of charge carriers making it preferable for detector design. Although all metal-semiconductor junction are Schottky in nature, Ohmic contact can be built via a reduction of potential barrier. Choosing metal and semiconductor combination of appropriate work functions

or heavy doping the surface of the semiconductor to reduce depletion width are two methods of Ohmic contact construction.

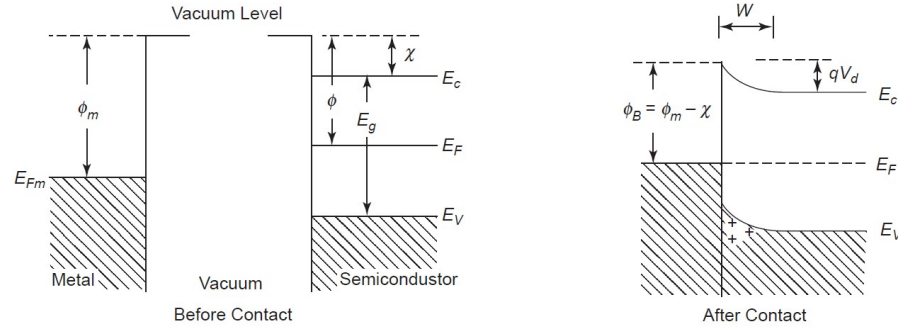


Figure 2.5: Energy level diagrams for a contact between a metal and an intrinsic semiconductor (or an insulator).  $E_g$  is the band gap,  $E_c$  is conduction band minimum,  $E_v$  is valence band maximum,  $V_d$  is the contact potential [62]

Due to negative electron affinity on H-terminated CVD diamond surface, Ohmic contact can be realized with high work function metal like Au, while Schottky contact can be formed with Al or Ni [63]. However the metal is not covalently bonded but rather weakly attached by Van der Waal forces [64]. For radiation detector application, O-termination is usually used in order to form adhesive metal contact to the diamond bulk. The dependence of metal electronegativities vanishes after oxygen termination [65]. Schottky contact on moderately doped/undoped can be formed by using wide range of metal including Al, Au, Ti and Cu [66]. In principle, Ohmic contact can be realized on highly doped diamond or sputter-induced physical damaged surface. A commonly employed technique for Ohmic contact is the deposition of the thin film of Ti, Cr, or Mo followed by Au coating and a post-metallization annealing in order to form a carbide at the diamond-metal interface on semiconducting diamond [67]. Direct deposition of Au or Pt has poor adhesion on the diamond surface, so the thin film of Ti, Cr, or Mo is needed as a middle layer. The carbide layer created from

post-metallization annealing contributed to low contact resistivity [67]. It is interesting to note that annealing process could change the rectifying contact of Al over to Ohmic contact at 700 °C caused by changes in surface bonding and band bending [68].

## Chapter 3

# Diamond as a Solid-State Particle Detector

Diamond as a wide-bandgap semiconductor has great advantages of being low leakage current, radiation-hard and high speed radiation detector. Diamond detector can response to any radiation that has enough energy to generate free carriers, including both electromagnetic radiation (UV, X-ray and  $\gamma$  rays) and high energy particle radiation ( $\alpha$  particles, electrons, neutrons and pions) [69]. In this work, the  $\alpha$  particles detection by using ScCVD diamond is particularly interested and the mechanism will be discussed in this chapter.

### 3.1 Interaction of Charged Particles

When a charged particle, such as  $\alpha$  particle, enters an absorbing medium, it immediately interacts simultaneously with many orbital electrons within the absorber atoms

via coulomb force. Part of energy of the charged particle is transferred to the electrons as encounters, resulting in decrease of velocity. The linear stopping power  $S$  for charged particles in a given absorber describes the continuously losing energy over the path

$$S = -\frac{dE}{dx} \quad (3.1.1)$$

The value of  $-\frac{dE}{dx}$  along a particle track is also called its specific energy loss. The classical expression of the specific energy lose is described by Bethe formula

$$-\frac{dE}{dx} = \frac{4\pi e^4 z^2 Z \rho N_A}{m_e v^2 \beta^2 A} B \quad (3.1.2)$$

where

$$B \equiv \left[ \ln \frac{2m_e c^2 \beta^2}{I(1 - \beta^2)} - \beta^2 \right] \quad (3.1.3)$$

$m_e$  is electron mass,  $v$  and  $z$  are the velocity and charge of the primary charged particle in unit of  $e$ ,  $A$  is the atomic weight of absorbing material,  $\rho$  is the density of absorber,  $\beta=v/c$  of the incident particle,  $m_e$  is the electron rest mass,  $N_A$  is Avogadro's number =  $6.022 \times 10^{23} \text{ mol}^{-1}$ ,  $Z$  is absorber's atomic number, and  $c$  is speed of light.  $I$  is an experimentally determined parameter of the average excitation and ionization potential of the absorber. For non-relativistic charged particles ( $v \ll c$ ), only the first term in equation 3.1.3 is significant.

Equation 3.1.2 is generally valid for different types of charged particles with relatively high energy provided their velocity remains large compared with the velocities of the orbital electrons in the absorbing atoms [37]. A more precise expression added Bloch's correction is referred as Behte-Bloch formula, which shows below with density

and shell effects corrections

$$-\frac{dE}{dx} = \frac{4\pi e^4}{m_e v^2} \frac{z^2}{\beta^2} \frac{Z\rho N_A}{A} \left[ \frac{1}{2} \ln\left(\frac{2m_e \gamma^2 v^2 W_{max}}{I}\right) - \beta^2 - \frac{\delta}{2} - \frac{C}{Z} \right] \quad (3.1.4)$$

where  $\gamma = 1/\sqrt{1 - \beta^2}$ ,  $\delta$  and  $C$  are density and shell correction which are important at high and low energy respectively, and  $W_{max}$  is the maximum energy transfer in a single collision, which is produced by head-on collision given by

$$W_{max} = \frac{2m_e c^2 \eta^2}{1 + 2s\sqrt{1 + \eta^2} + s^2} \quad (3.1.5)$$

where  $s = m_e/M$ ,  $M$  is the mass of the incident particle, and  $\eta = \beta\gamma$ .

Bethe-Bloch stopping power formula indicates the rate of energy loss in a given material is determined by the velocity and the charge of the primary charged particle. The specific energy loss varies as  $1/v^2$  for non-relativistic charged particles, or inversely proportional to the energy. The  $dE/dx$  decreases with increasing velocity until reaching the minimum ionizing point. As the energy increases beyond this point, the logarithmic part dominates and  $dE/dx$  rises again. If comparing particles with the same velocity,  $z^2$  is getting dominating in equation 3.1.2 which means particles with greater charge will have larger energy loss. In addition, the electron density of the absorber determined by the product of  $NZ$  also effect the specific energy loss. Thus, the energy loss of charge particles in diamond (carbon) is less than silicon which makes diamond with better particle transmission capacity.

For a heavy charged particle such as an alpha particle with few MeV initial energy, the rate of energy loss keeps increasing at a rate of  $1/E$  as kinetic energy decrease, so more energy per unit length will be deposited toward the end of the track as specific

energy loss increases. In the end of the track, the charge of the charge particle is reduced through electron pickup which refers to the behavior of nuclear fragments pick up electrons from the material as it slow down. The specific energy loss decrease as charge reduced which results in a peak drop off of the stopping power. This feature reflected in a plot of stopping power as a function of penetration depth is called Bragg curve.

The range of a charged particle can tell the path length over which the initial energy is exhausted. The continuous slowing down approximation (CSDA) range of a particle of a given initial energy  $E_0$  is defined as

$$R = \int_0^{E_0} \left(\frac{dE}{dx}\right)^{-1} dE \quad (3.1.6)$$

The energy loss of a particle in a material is not in fact continuous, but statistical in nature [70]. There is a statistical distribution of the mean range known as range straggling. The range for 5.5 MeV  $\alpha$  particle in diamond is about 16  $\mu m$ .

## 3.2 Charge Carrier Generation

The part of energy loss of the incident particle in semiconductors is used to create electron-hole pairs which are collected at electrode to produce electronic signal. The average energy to create one electron-hole pair is loosely called the ionization energy or W-value  $\epsilon$ . The energy required for carrier generation in semiconductors is much less than in typical gas-filled detector, thus semiconductor detectors have better energy resolution as a dominant advantage. The W-value is approximately three times the band gap energy for semiconductors. The W-value for diamond was measured as 13.2

eV [71]. The number of electron-hole pairs generated in the semiconductor  $n$  due to ionizing energy deposited from incident particle with energy  $E$  can be written as

$$n = \frac{E}{\epsilon} \quad (3.2.1)$$

In planar geometry device which has metal-semiconductor-metal configuration, electron-hole pairs generated by W-value are separated by electric field when voltage is applied on the metal contacts. The motion of the charge carriers induces current in the external circuit as pulse signal. Shockley-Ramo Theorem gives the relationship of instantaneous current  $i$  induced on a given electrode due to the motion of a charge

$$i = qvE_0 \quad (3.2.2)$$

where  $E_0$  is the weighting field determined by applying unit potential to the electrode that is for the charge calculation, and all other electrodes are set to zero. In the planar device, only two electrode pads in a sandwich configuration, thus  $E_0 = 1/W$  where  $W$  is the distance between electrodes.  $v$  is the velocity of the charge carrier which relates to charge carrier mobility  $\mu$

$$v = \mu\varepsilon = \mu \frac{V}{W} \quad (3.2.3)$$

where  $\varepsilon$  is electric field. so the collection time of an electron traveling  $x$  from where it excited to an electrode is given

$$t = \frac{x}{v} = \frac{W^2}{\mu V} \quad (3.2.4)$$

Then substitute equation 3.2.3 and 3.2.4 into 3.2.2, the induced charge collected at the electrode if there is  $n$  electron-hole pairs presenting can be expressed as

$$Q_{ind} = it = qn \frac{x}{W} \quad (3.2.5)$$

the product of  $qn$  is  $Q_{gen}$ , the charge generated. Equation 3.2.5 can be rewritten into

$$\frac{Q_{ind}}{Q_{gen}} = \frac{x}{W} \quad (3.2.6)$$

$\frac{Q_{ind}}{Q_{gen}}$  is also called the charge collection efficiency (CCE), a figure of merit for the characterization of CVD diamond detectors.  $x$  is referred as charge collection distance (CCD). This implies the charge collection efficiency is proportional to the ratio of CCD and thickness of the semiconductor bulk. In the case that  $CCD < W$ , only a fraction of charge will be collected and the uncollected charge can result in the accumulation of a net charge within the device which may cause the distortion of electric field [69]. The CCD can be calculated from the product of charge carrier mobility  $\mu$ , carrier lifetime  $\tau$  and electric field  $E$

$$x = \mu\tau E \quad (3.2.7)$$

Depending on crystal quality and type of the diamond, the CCE of diamond can be reaching 100% for nature IIa type diamond and spectroscopic grade ScCVD diamond while it can be as low as 40% for polycrystalline CVD diamond and detector grade ScCVD diamond [72, 73]. The impurities and crystal defects can cause trapping and recombination of the carrier which will decrease the lifetime. The product of  $\mu\tau$  of high purity single crystal CVD diamond is 2 to 3 orders of magnitude greater than polycrystalline diamond [74]. A nearly 100% CCE of high quality single crystal CVD

diamond is experimentally determined [75, 45, 73].

The average charge carrier lifetime of single crystal CVD diamond is about a few microsecond ( $10^{-6}$ s) [76] and it is shorter compared with silicon (typically a few milliseconds). Since typical collection time for the carriers is of the order of  $10^{-7}$  to  $10^{-8}$  s [37], the relatively short carrier lifetime of CVD diamond may result in insufficient charge collection.

### 3.3 Impurities and Dopants

In intrinsic semiconductors, the number of electrons in the conduction band is exactly equal the number of holes in the valence band. The equilibrium concentration of electrons (or equally holes) in an intrinsic semiconductor is

$$n_i = \sqrt{N_c N_v} \exp\left(\frac{-E_g}{2kT}\right) \quad (3.3.1)$$

where  $N_c$  and  $N_v$  are number of states in conduction band and valence band respectively,  $E_g$  is the energy gap at 0 K and  $k$  is the Boltzmann constant. Typical value of  $n_i$  is on the order of  $1.5 \times 10^{10} \text{cm}^{-3}$  for silicon,  $2.5 \times 10^{13} \text{cm}^{-3}$  for germanium and  $10^{-27} \text{cm}^{-3}$  for diamond. As a result of very low  $n_i$ , diamond has extremely low leakage current at normal condition. In practice, the intrinsic semiconductors is virtually impossible to achieve due to the existing of small amount of residual impurities. The small concentrations of impurity (in the order of a few parts per million or less) largely dominates the property of the semiconductor.

When impurities are intentionally implement into the material to tailor its properties, it is called dopant for doped semiconductor. For tetravalent semiconductors

material like carbon, silicon and germanium, if the impurity incorporated is pentavalent (e.g. group V elements), then its extra valence electron will be left out the band. In this case, the impurities are called donors. The level of the donors is just slightly below the conduction band and the electrons can be easily excited into it. The current in such material is mainly due to the movement of electrons (major carriers) and less from holes (minor carriers). This kind of semiconductors is referred as n-type semiconductor. If the doped impurity is trivalent (e.g group III) which has one less valence electron, there will be an excess of hole in the crystal. An acceptor level is then created close to the valence band and electrons from the valence band can easily excited into this extra band leaving extra holes behind. The semiconductors in which holes are the majority carriers are called p-type semiconductors.

In nature diamond, boron and nitrogen are commonly found which makes diamonds appearing enchanting colors. Boron has been implanted successfully into CVD diamond to make p-type semiconducting diamond. Boron has three valence electrons, thus it plays as acceptors, although it is not a shallow acceptor due to the  $W$ -value of 0.37 eV from conventional point of view. The resistivity of boron-doped diamond is significantly smaller than intrinsic diamond. Nitrogen can be considered a donor since it is tetravalent, but its  $W$ -value is far too great for it to be a useful donor (1.7 eV) [77]. The nitrogen impurities introduce an energy level near the middle of the forbidden band which may trap the movement of carriers. The only feasible n-type semiconducting diamond is doped with phosphorous with a donor level of 0.6 eV.

### 3.4 Trapping and Recombination

When electron-hole pairs are generated in the semiconductor, ideally we want them to migrate under electric field until they are collected at electrodes to achieve full charge collection. However, due to the presence of deep impurities which have relatively high W-value and lie in the middle of forbidden band, the charge carriers could be trapped and recombine sometime before arriving the electrode.

Deep impurities can trap carriers which means a electron or hole is capture and hold for a while. The trapping usually causes sufficiently long delay on the carriers' movement, preventing the form of electronic pulse formation the charge carriers. when significant trapping occurs, the induced charge becomes a function of the distance over which the charges travel [37]. Then instead of equation 3.2.5, Hecht's relationship is applied

$$Q_{ind} = qn \left[ \frac{v\tau}{W} (1 - \exp(\frac{-x}{v\tau})) \right] \quad (3.4.1)$$

If the trappings occur inhomogeneously by short-range ionization, a local space charge distribution would build up an internal electric filed in a opposed way of applied field. This phenomenon is called polarization which will progressively deteriorate the pulse height measurement. For traversing particles and with prolonged irradiation time, the number of empty traps will be reduced and traps tend to be distributed homogeneously. As the result, the polarization seems to be absent (in case of low ionizing particles such as electrons) or less important (in case of heavier particles like proton or alpha particles) [78]. This effect is called primming or pumping which increases the collection efficiency. The polarization and priming effect is commonly seen in diamond radiation detector, especially polycrystalline diamond due to presence of

high ratio of  $sp^2/sp^3$  phase in form of grain boundaries [79].

Recombination is similar to the trapping. When one type of carrier is hold, for example, electron, it may be released back into the conduction band or combine with a hole coming slightly later then annihilate. Once the recombination process is finished, the impurity site return to its original state and can start another recombination. The mean charge carriers lifetime decreases due to the recombination.

# Chapter 4

## Fabrication of the Ultra-thin ScCVD Diamond detector

The producer of the detector fabrication in this work was developed from Tong's experiences [29]. Some technique improvements have been applied in order to prepare an ultra-thin ScCVD diamond detector.

### 4.1 Commercial ScCVD Diamond

For CVD diamond detector application, although it is possible to grow CVD diamond crystal at home facilities [80], purchasing commercially available CVD diamond plates from a company like Element Six and then fabricating to detectors in need is much more convenient.

The single crystal CVD diamond sample used in this work was purchased from Applied Diamond Inc, Wilmington, USA. The purchased ScCVD diamond was an optical grade single crystalline square plate with a dimension of 3 mm×3 mm×50

$\mu\text{m}$  grew in microwave plasma CVD reactors. Optical grade is relatively cheaper than electronic grade CVD diamond but with a little bit higher nitrogen concentration (substitutional  $[\text{N}] < 1$  ppm) compared to  $[\text{N}] < 5$  ppb for electronic grade ScCVD diamond which is suitable for spectroscopic application. Optical grade ScCVD diamond had been successfully proved as a radiation detector [45]. A customized  $3\text{ mm} \times 3\text{ mm} \times 500\ \mu\text{m}$  polycrystalline CVD diamond membrane with a 2 mm diameter hole in the center was ordered from Applied Diamond as a mask for plasma etching procedure.

## 4.2 Plasma Etching

For a transmission-type alpha particle detector, the thickness of the CVD diamond sample should be less than  $10\ \mu\text{m}$  to allow alpha particle traversing with sufficient energy remained. The commercial ScCVD diamond plate purchased from Applied Diamond was  $50\ \mu\text{m}$  so it must to be further thinned down. A STS 320PC Reactive Ion Etch (RIE) System at the Center of Emerging Devices and Technology (CEDT) at McMaster University was used to etch down the ScCVD diamond plate. The general mechanism is to use plasma generated from the mixture of gases hitting on the substrate and chemical reaction between the substrate material and plasma produces volatile etch products that modify the surface of the target substrate.

Carefully placed the  $50\ \mu\text{m}$  ScCVD diamond plate on the base of the cylindrical vacuum chamber by using a plastic tweezers and then covered the ScCVD diamond plate with the customized  $500\ \mu\text{m}$  PcCVD diamond mask. The PcCVD diamond mask allowed the plasma etching down the uncovered part of ScCVD diamond plate along the hole and kept the covered part remaining untouched for easy handling. Since the

mask was also made by CVD diamond, contamination can be avoided. The process parameters of the etching were summarized in Table 4.1. The etching process was taken for 45 hours and aborted for thickness exam measured by a stylus profilometer which indicated etched thickness  $37\ \mu\text{m}$ . To approach the thinner sample, another 8 hours was performed ended up with approximated  $44.7\ \mu\text{m}$ . The etching rate was about  $0.84\ \mu\text{m}/\text{h}$ .

Parameters	Set values
Oxygen flow rate	8.0 sccm
Argon flow rate	3.2 sccm
RF Power	400 W
Pressure	20 mTorr
Base pressure	10 mTorr
Cooling Temperature	20 °C

Table 4.1: Process Parameters Values of RIE operation

The stylus profilometer provided an approximate thickness. For more accurate measurement, an Alicona InfiniteFocus G5 optical measurement system at McMaster Manufacture Research Institute (MMRI) was used. This system measurement the surface based on the technology of detecting different optical reflectance values when it scans the surface. The optical profiles of each side of the etched ScCVD diamond plate show in Figure 4.1. The images showed both sides of the plate was etched because the diamond plate slide was accidentally flipped for the second etching session. Due to double-side etching, the optical measurement had to be done for each slide separately, otherwise the optical focus can not be measured properly. The curves

on top represent the thickness profile along the red line indicated on the optical images below. The fluctuation shown in the trough indicated imperfect flatness in plasma etching. There were some large fluctuations around the peaks which caused significant errors in the thickness determination. The difference in thickness on each side calculated by averaging over the profiles was  $23.891 \pm 9.528$  and  $19.051 \pm 7.088 \mu\text{m}$  respectively. Thus, the thickness of the thinned part of the ScCVD diamond plate was  $7.058 \pm 11.876 \mu\text{m}$ . Due to the large error, this thickness value is for reference.

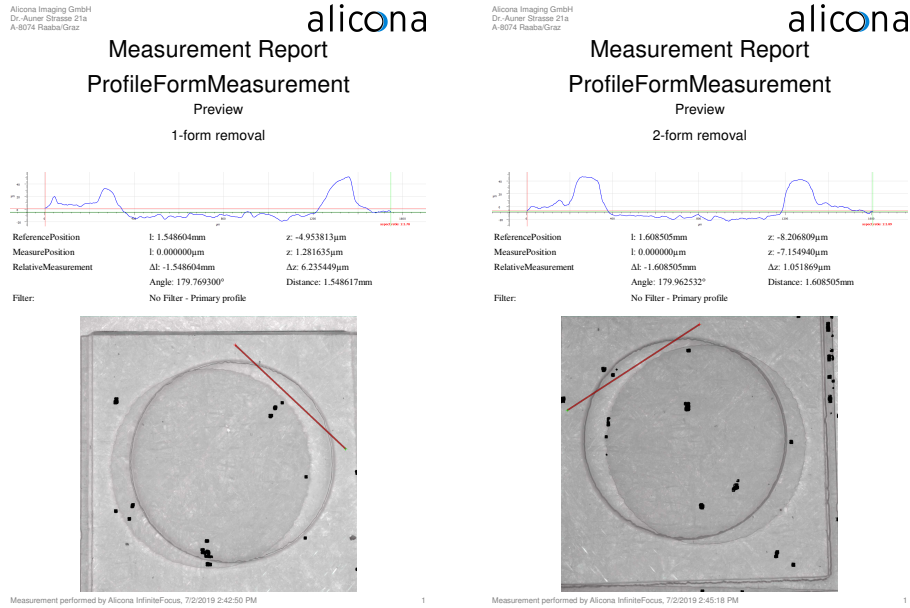


Figure 4.1: Alicona measurement profiles of each side of etched ScCVD diamond plate

### 4.3 Cleaning

Cleaning is an essential step for CVD diamond detector fabrication with two purposes. One is to remove the contamination during handling and plasma etching and another

is to oxide the diamond surface (O-termination) for adhesive metal contact.

The etched ScCVD diamond sample was cleaned in the cleaning room at CEDT, followed the RCA-2 Standard Clean protocol which was developed by Werner Kern at Radio Corporation of America (RCA) laboratory [81]. The procedure was that first put 6 parts deionized (DI) water into a beaker and added 1 part of HCl solution (27%). Then heated the solution to 75 °C on a hot plate. Removed the beaker from the hot plate and added 1 part H<sub>2</sub>O<sub>2</sub> (30 %) solution. Waited couple minutes until bubbles appeared. Carefully soaked the diamond sample in the solution for 10 mins by using a Teflon basket with small holes. Rinsed the sample in DI water. Finally, dried the sample and sealed in a clean plastic vessel to avoid contamination.

## 4.4 Electrodes Fabrication

Squared electrodes in parallel geometry were sputtering by a Torr International Inc. CRC 600 machine at CEDT. To sputter selective are of the diamond avoiding metal residues on the edges, a 3×3 cm shadow mask with 2×2 mm opening was manufactured at McMaster Research Machine Shop by 0.8 mm thick brass sheet. A holder with an approximately 50 μm depth 3×3 mm squared shallow indentation was manufactured by laser engraving on an aluminum 6061 block at McMaster Learning Factory in order to demobilize the diamond sample when used the shadow mask. Figure 4.2a demonstrates the mask and holder which can be used in vacuum environment with no contamination. For the sputtering, used a plastic tweezer to take out the cleaned diamond sample from the vessel and placed the diamond in the holder and covered the mask on it fixing with Kapton tapes.

Installed gold target on the RF gun and chromium target on the DC gun of the

sputtering machine. Initiated the machine to start vacuuming until the base pressure reaching  $10^{-5}$  Torr level. Set argon flow at 6 sccm, turned on DC module to set voltage 380 V and current 80 A to deposit 500 Å (50 nm) Cr and then used RF power at 80 W to deposit 1500 Å (150 nm) Au contact. The metal deposition rate is about 1 Å/s. Repeated again for another side of the diamond sample. Post-metallization annealing was done at 550 °C in argon atmosphere for 15 minutes using JetFirst Rapid Thermal Anneal at CEDT. The annealing process created a carbide interface for Ohmic contact formation and it works as a middle layer increasing the adhesion of metal on the diamond surface. Figure 4.2b shows the ultra-thin ScCVD diamond sample with Au/Cr contacts after annealing. The Au/Cr coating and post-metallization annealing produced an Ohmic contact on the diamond beneficial for signal transmission.

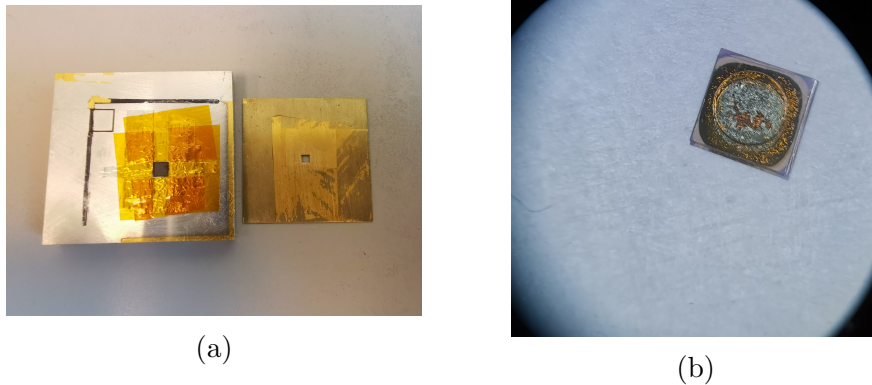


Figure 4.2: (a) The laser engraved aluminum holder (left) and brass mask (right) for selective sputtering (b) Metalized ultra-thin ScCVD diamond with Au/Cr contacts after annealing, image was taken under 10X microscope

## 4.5 Electronic Assembling

A customized print circuit board (PCB) with a 2 diameter hole in the center was used as the host of the diamond sample. One side of the ultra-thin ScCVD diamond sample was glued above the hole of the PCB by Super Shield silver conductive coating from M.G Chemical. The up side of the diamond was connected into the circuit by a piece of flat copper wire one end glued on the ScCVD diamond electrode via silver paint and one end welding on the PCB. Gently and carefully removed extra silver coating residual from the surface of diamond sample by precision brush with acetone solution to secure the insulation between the anode and cathode.

The PCB was installed on as shown in Figure 4.3 as a detector inside an aluminum chamber as electrostatics shield which connects to a SHV connector for biasing and signal readout via a coaxial cable. Teflon tapes were wrapped on exposed copper of the PCB to reduce potential high voltage danger during biasing.

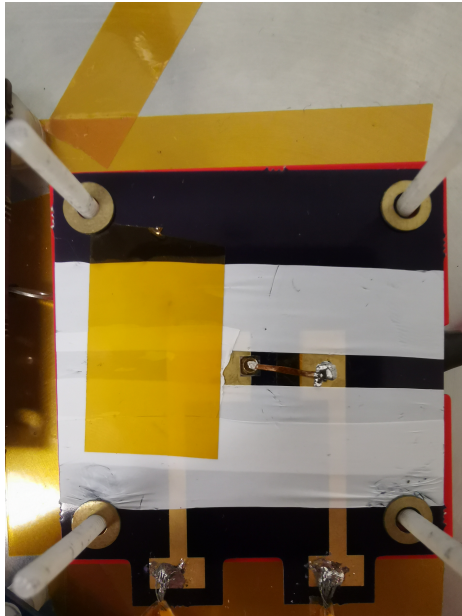


Figure 4.3: The ultra-thin ScCVD diamond detector mounted on a PCB and assembled as a detector

# Chapter 5

## Computational Modeling of the ScCVD diamond detector

Computational modeling is important for detector design. There are two simulations had been conducted to study the characteristic of ScCVD diamond detector as a transmission-type alpha detector. SRIM (the Stopping and Range of Ions in Matter) was used to calculate the energy loss of  $\alpha$  particle in diamond detector for different electrodes. MCNP (Monte Carlo N-Particle transportation code) 6 simulations were applied to predict the detector performance in experimental setup.

### 5.1 SRIM Calculation

#### 5.1.1 Method

Alpha particle ( ${}^4\text{He}^{2+}$ ) is highly ionizing radiation but with very weak penetration depth. For 5.5 MeV  $\alpha$  particles, they can only travel 3.7 cm in air or stopped by a

piece of paper. The penetration depth is closely related to the density of material. Thus, Special care must be paid in the transmission-type alpha detector design.

Previously work done by Tong [29] demonstrated the feasibility of fabricating a thin ScCVD diamond detector with 400nm aluminum electrodes deposited by sputtering. Aluminum is a common electrode material which has great conductive and low cost. Aluminum on O-terminated diamond surface forms Schottky contact. In order to construct Ohmic contact for better signals collection, gold and Chromium are generally used. In addition, aluminum thin film could be easily peeled off because it not strongly covalently bonded on the diamond by weakly attached via Van der Waal force [64]. Consider the denser density of gold and chromium compared to aluminum, the energy loss of alpha particles in different electrodes need to be investigated.

SRIM is a collection of software package that can quickly calculate the mass stopping power  $\frac{S(E)}{\rho}$  [ $cm^2MeV/mg$ ] of a given ion in matters in table formats [82]. The mass stopping power data was exported from SRIM and fitted into a polynomial function of incident energy  $E$  [83] below to obtain the coefficients  $a_0$ ,  $a_1$ ,  $a_2$  and  $a_3$  by MATLAB

$$\frac{\rho}{S(E)} = a_0 + a_1E^{-0.4} + a_2E^{0.25} + a_3E^{0.8} \quad (5.1.1)$$

Following the definition of stopping power  $S(E)$  (equation 3.1.1), the length of a particle with initial energy  $E_i$  traversing through a material ending up with final energy  $E_f$  can be calculated

$$L = \frac{1}{\rho} \int_{E_f}^{E_i} \left( \frac{\rho}{S(E)} \right) dE \quad (5.1.2)$$

where  $\rho$  is the density [ $mg/cm^3$ ] of the material. Substituted equation 5.1.1 with all

coefficients into equation 5.1.2

$$(a_0 E_i + \frac{a_1}{0.6} E_i^{0.6} + \frac{a_2}{1.25} E_i^{1.25} + \frac{a_3}{1.8} E_i^{1.8}) = (a_0 E_f + \frac{a_1}{0.6} E_f^{0.6} + \frac{a_2}{1.25} E_f^{1.25} + \frac{a_3}{1.8} E_f^{1.8}) + L\rho \quad (5.1.3)$$

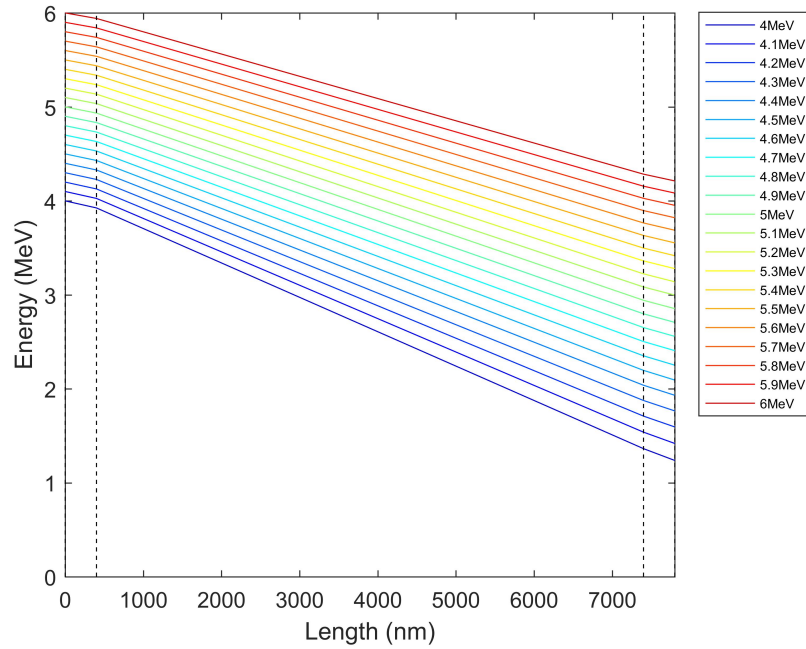
$L$  here is the thickness of the material. Solve the equation for the final energy  $E_f$  and then the energy loss of particles in a certain material can be calculated as  $E_f - E_i$ . The final energy will be the initial energy for the next material. The calculations will be performed material by material in a chain.

Assumed the diamond thickness is  $7 \mu m$  and  $400 nm$  aluminum contact on each side of the diamond. The thicknesses of Au and Cr were  $100 nm$  and  $50 nm$  respectively on each side.

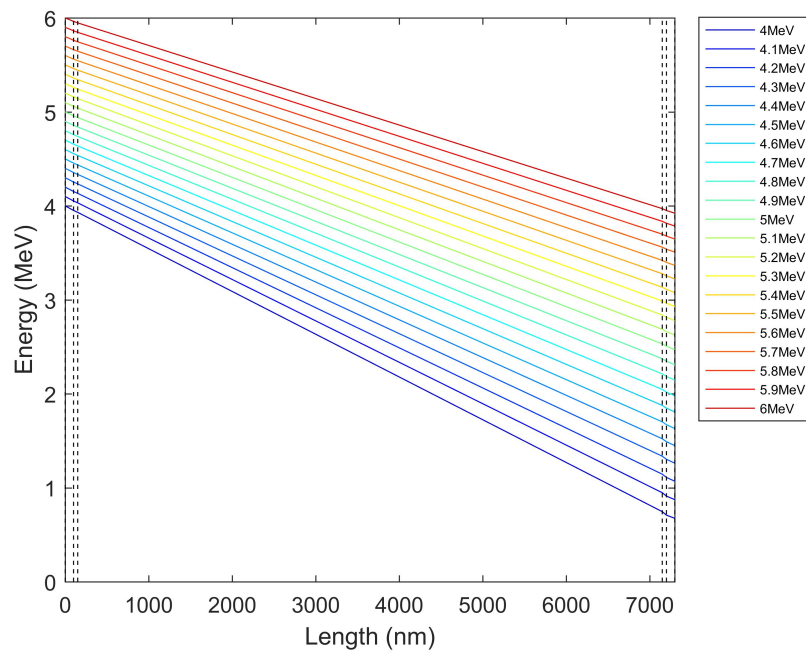
## 5.1.2 Results

The results of energy loss of alpha particles from  $4 MeV$  to  $6 MeV$  in Al and Au/Cr electrodes are shown in Figure 5.1. As incident energy increases, the energy loss of alpha particles in diamond decreases due to incident energy dependence of stopping power. The total energy loss in Al and Au/Cr contacts ranges from  $0.13$  to  $0.20 MeV$  and  $0.10$  to  $0.14 MeV$  respectively.

Therefore, The energy loss of alpha particles in energy range from  $4$  to  $6 MeV$  in both types of electrodes are quite comparable. Although alpha particles lose more energy per length in Ar/Cr than Al, the thinner film of Cr/Au made the compensation. The energy loss in electrodes only accounts for about  $5\%$  of the total loss while the majority energy deposits in the diamond. Thus, the change of contact metal will not impact on the overall transmission performance of the diamond detector.



(a) Al electrodes



(b) Cr/Au electrodes

Figure 5.1: Energy loss of alpha particles through Al and Cr/Au electrodes. The dash lines represent the boundary of materials

## 5.2 MCNP Simulations

### 5.2.1 Introduction to MCNP

The Monte Carlo method in particle physics is a computational method that simulates the behavior of particles. The birth of Monte Carlo method can be traced back to 1940s, the development of the first atomic bomb during World War II. In order to solve the complex neutron diffusion, transport and multiplication problems which have many highly complicated integrals involved, a mathematical method with statistical sampling technique ran on the first generation of computer was invented by Von Neumann with Ulam, Fermi, Metropolis and other at Los Alamos National Laboratory (LANL), NM, USA. The Monte Carlo method was then further developed as a general-purpose, continuous-energy, generalized-geometry, time-dependent, Monte Carlo radiation-transport Fortran-based code by LANL and known as Monte Carlo N-Particle code (MCNP) nowadays [84]. MCNP6 is the latest version of MCNP code described as the merger of MCNP5 and MCNPX. MCNP is primarily for neutron transport simulation, MCNPX adds simulation ability to wide range of particles including ions, baryons and leptons.

### 5.2.2 Method

To execute MCNP, an input file as description of the problem is required. The input file includes Cell Card and Surface Card for geometry construction, and Data Card which has source, material and tally specification.

### Source-CVDD-SBD configuration

The geometry of source-CVD Diamond (CVDD) setup was visualized as shown in Figure 5.2a. In this setup, Cell 12 represents an disk source sealed with platinum and Cell 1 is the active volume. Cell 2 is a source holder made by Rexolite (polystyrene) and it also works as a collimator with 15 mm radius. Cell 3 is the ultra-thin CVDD membrane with 50/150 nm Cr/Au electrode coatings on both sides. In order to acquire simulation results closer to the real case, an etched CVDD was configured in MCNP. There was a sunken 2 mm diameter circle in the center of the diamond, Figure 5.2b shows the cross section view. There is a sunken indentation part ( $7\ \mu\text{m}$ ) in the middle while the "highland" parts has  $50\ \mu\text{m}$  thickness. The Au/Cr contact coats over the whole indentation and partial surface of the "highland". Cell 8 is a printed circuit board (PCB) mainly made by Fiberglass grade E with a 1 mm radius hole at the center. Cell 100 is the interested area filled with dry air. A  $\Delta E$ -E detectors setup shown in Figure 5.2c consisting a silicon Surface Barrier Detector (SBD) beneath the CVDD. Cell 9 represents an silicon SBD with 11 mm diameter of the silicon crystal. All material composition information was referred to [85] for material cards.

A 5.4 MeV alpha particle point source was used to discovery the energy deposition throughout the CVDD and in the SBD. An isotropic disk volume source was defined inside Cell 1 in order to simulate experimental result.

F8 and \*F8 tally were applied to simulate pulse height spectrum and energy deposition in the Cells. An important input for simulating alpha particles is CUT:a command. MCNP will automatically cut information if alpha energy is lower than 4 MeV. Without modify this, most of information for the spectrum will be lost. Thus,

Used command for all the simulation:

$$CUT : a j 0.001 j j \quad (5.2.1)$$

to force the MCNP keeping calculation for alpha energy as low as 0.001 MeV.

### Microbeam configuration

The ultra-thin diamond detector can work as the vacuum window on top of the final beam-line collimator at microbeam end-station. Figure 5.3a demonstrates the key geometry in a upside down direction. The microbeam at McMaster University Biological Microbeam Facility was originally from RARAF, Columbia University which used a double apertures collimator to focuses the beam. One of the final beam-line collimator at McMaster made by stainless steel contains two  $5 \mu\text{m}$  laser drilled holes separated by a  $1025 \mu\text{m}$  spacer illustrated by Figure 5.3b where the exit angle  $\theta$  is

$$\theta = \cos^{-1}\left(\frac{5}{1025}\right) = 0.28^\circ \quad (5.2.2)$$

Cell 100 indicates vacuum environment inside the collimator. The ultra-thin CVDD same as in Figure 5.2b locates on the exit of the collimator working as a transmission-type detector and a vacuum window represented by Cell 3. A  $2 \mu\text{m}$  thick polypropylene petri dish is placed 1 mm below the CVDD. A human Eukaryotic cell sample with  $20 \mu\text{m}$  radius and  $3 \mu\text{m}$  thickness is on the petri dish. Cell 9 is the silicon SBD locates 0.5 mm beneath the petri dish. Cell 12 is the air gap covering the petri dish, cell sample and SBD. The SBD is used to check the energy remained after the source particle passing through the cell sample. All material composition information was

referred to [85] for material cards.

The source specification assumed a 4/6 MeV  ${}^4\text{He}^{2+}$  beam with 6  $\mu\text{m}$  diameter. A monodirectional beam was defined for energy loss in the CVDD and deposition in the cell sample. A  $\cos\theta$  distribution between incident angle 0 and  $0.28^\circ$  was applied to simulate more realistic scenario. F8 tally is used to simulate pulse height spectrum in the CVDD and SBD. \*F8 tally was used for energy deposition in the each Cell.

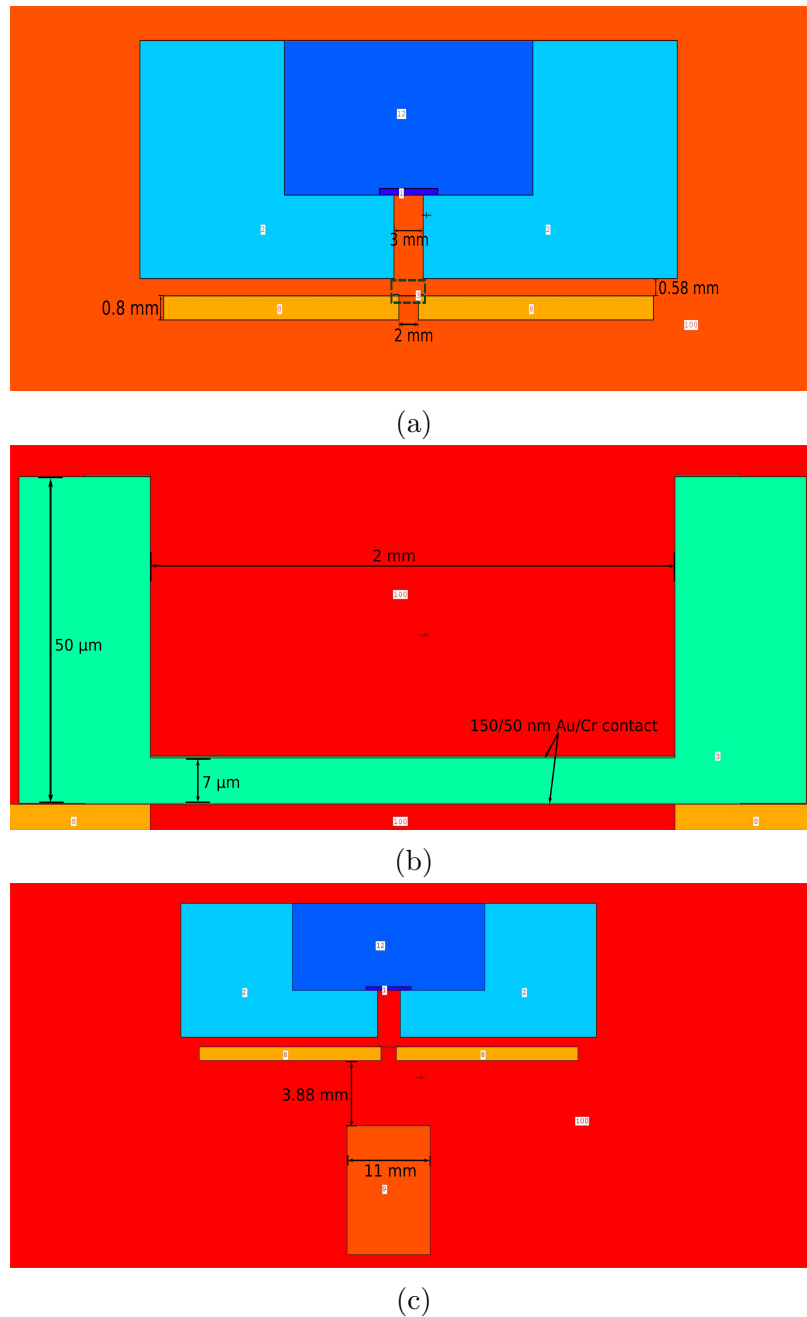
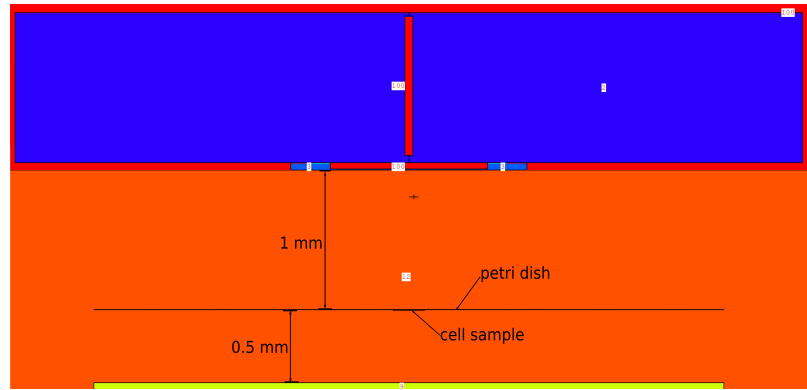
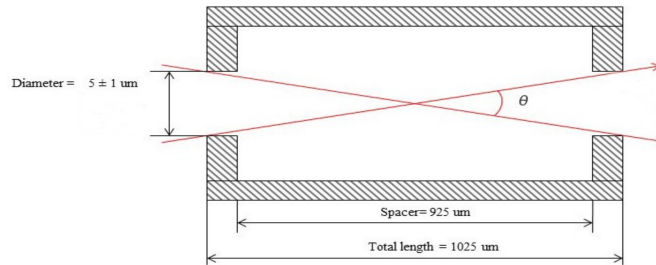


Figure 5.2: (a) MCNP configuration of the source-CVDD in cross-section view visualized by VISED (b) geometry detail of diamond and metal contacts as the zoomed in of the dashed box in (a) (c) source-CVDD-SBD ( $\Delta E$ -E setup) in cross-section view visualized by VISED. Cell 1: active volume of 5.4 MeV alpha particle disk source, Cell 12: the disk source, Cell 2: the source holder, cell 3: the diamond membrane, Cell 8: PCB, Cell 9: silicon SBD and Cell 100: air. Sizes and distances are not to scale



(a)



(b)

Figure 5.3: (a) MCNP configuration of the CVDD as a vacuum window at microbeam end-station in cross-section view visualized by VISED. Cell 2: the final beam-line collimator, cell 3: the diamond membrane, Cell 9: silicon SBD, Cell 12: air and Cell 100: vacuum. (b) the schematic layout of the collimator (Cell 2) with dimensions. Sizes and distances are not to scale

### 5.2.3 Results

#### Source-CVDD-SBD configuration

Table 5.1 energy deposition in each compartment in the air was calculated by \*F8 tally. With the monodirectional point source specification, a 5.4 MeV alpha particle vertically goes throughout the hole of the source holder, and then directly penetrate

through the metal contacts to the diamond membrane, and deposit all the remaining energy in the silicon detector in the end.

Cell	Material	Energy deposition (MeV)
Cell 5	Au	$4.43 \times 10^{-2}$
Cell 4	Cr	$6.57 \times 10^{-2}$
Cell 3	CVDD	2.08
Cell 6	Cr	$2.11 \times 10^{-2}$
Cell 7	Au	$8.02 \times 10^{-2}$
Cell 9	Silicon	2.24
Cell 100	Air	$8.68 \times 10^{-1}$

Table 5.1: Energy deposition of a 5.4 MeV alpha particle in Cells of Source-CVD-SBD configuration

The energy loss of a 5.4 MeV alpha particle in the 7  $\mu\text{m}$  diamond is 2.08 MeV. The result of energy loss in diamond from SRIM calculation is 2.2 MeV. The total energy absorbed by metal contacts is 0.21 MeV which is about 10% of the energy deposited in the diamond and it is higher than 6% found in SRIM calculation. A reason for the discrepancy is that a small portion of energy had lost in air before arriving the metal contact in MCNP scenario which reduce the incident energy upon the diamond detector. As the consequence, lower incident energy means higher stopping power and more energy loss in the material .

The pulse height spectrum of CVDD and SBD was plotted in Figure 5.4 by using F8 tally with a 5.4 MeV isotropic disk source. Since MCNP tally output is automatically normalized to per particle, the output needs to multiple the number of particle to get counts. The counts data was then normalized regarding the maximum count

to convert into yield. There are three peaks can be identified from the blue spectrum representing the pulse height response of the CVDD. The left-hand side peak spanning from 2 to 3 MeV with the maximum yield at around 2.14 MeV is from the 7  $\mu\text{m}$  sunken indentation of the CVDD where only partial energy deposits in the diamond membrane. The shape of this peak has characteristics of Landau distribution which describes the energy straggling for heavy particles passing through a thin absorber [86]. The other two peaks on the right are very close to each other locating at about 5 MeV which may be the pulse response from the "highland" and the edge between the indentation and "highland". Because the thickness of the "highland" part is 50  $\mu\text{m}$ , full energy of the alpha particle will be deposited. The pulse height response of the silicon SBD represented as the red spectrum in Figure 5.4. The maximum yield of the SBD peak locates at around 2.18 MeV. It is notable that the total number of particles entering CVDD and SBD is not identical in this MCNP simulation. The ratio between particle population in CVDD and SBD is 3.67. For a  $\Delta\text{E-E}$  detector system, 100% hitting efficiency is usually expected. However, due to the presence of PCB acting as a secondary collimator, only 27.3% of particles entering CVDD could hit the SBD.

The  $\Delta\text{E-E}$  MCNP simulation results determined that a 7  $\mu\text{m}$  CVDD fabricated by plasma etching and Au/Cr metallization can be used as a transmission-type solid state detector for 5.4 MeV alpha particles. The pulse height spectrum of CVDD-SBD provided a prediction and reference for the experiments.

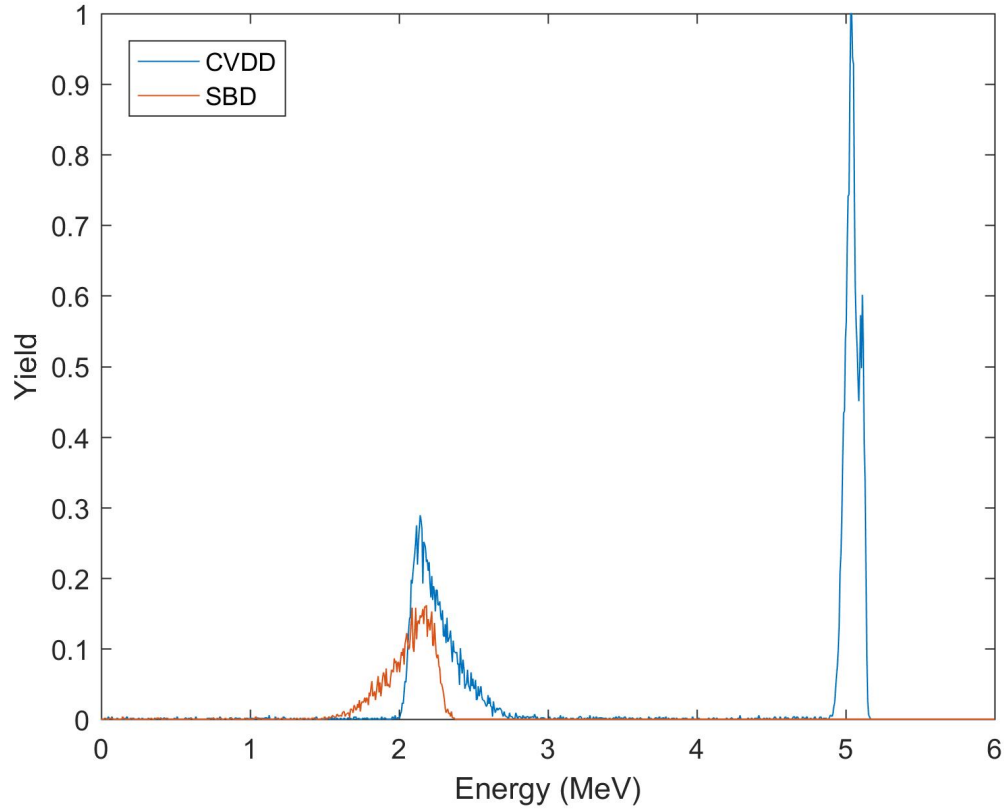


Figure 5.4: CVDD-SBD  $\Delta E$ -E MCNP pulse height spectrum

### Microbeam configuration

The ultra-thin ScCVDD membrane can be used as a vacuum window while can provide particle counting information. The energy loss of a monodirectional 4 and 6 MeV alpha particle in each Cells under the condition described previously shows in Table 5.2.

Cell	Material	Energy deposition (MeV)	
		4 MeV	6 MeV
Cell 5	Au	$7.33 \times 10^{-2}$	$6.16 \times 10^{-2}$
Cell 4	Cr	$1.88 \times 10^{-2}$	$1.50 \times 10^{-2}$
Cell 3	CVDD	2.70	1.81
Cell 6	Cr	$2.70 \times 10^{-2}$	$1.81 \times 10^{-2}$
Cell 7	Au	$9.07 \times 10^{-2}$	$7.22 \times 10^{-2}$
Cell 10	Petri dish	$4.70 \times 10^{-1}$	$2.14 \times 10^{-1}$
Cell 11	Eukaryotic cell	$4.35 \times 10^{-1}$	$3.46 \times 10^{-1}$
Cell 9	Silicon	$1.45 \times 10^{-2}$	3.31
Cell 12	Air	$1.70 \times 10^{-1}$	$1.50 \times 10^{-1}$

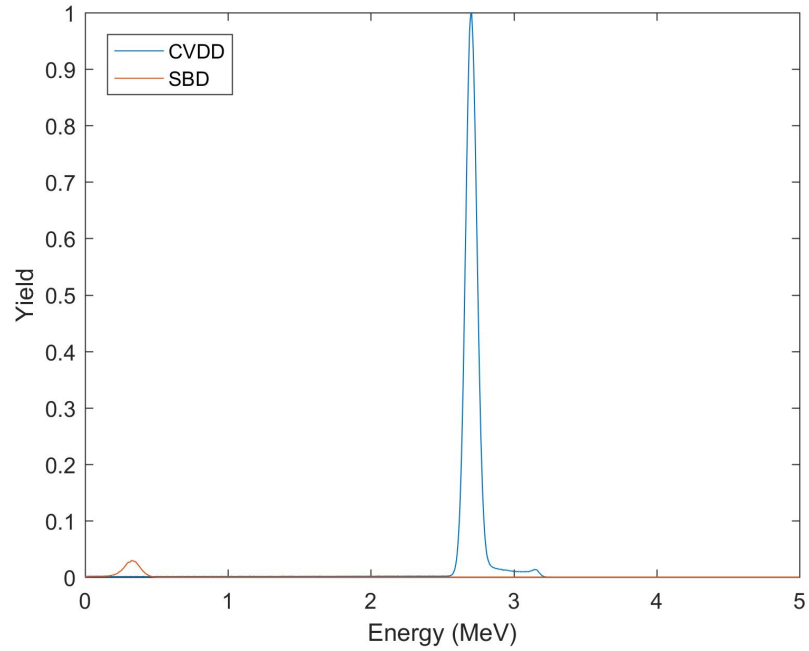
Table 5.2: Energy deposition of a 4/6 MeV alpha particle in Cells of microbeam configuration

With No surprise, 4 MeV alpha particle is going to lose considerably more energy in the  $7 \mu\text{m}$  CVDD beam window compared to 6 MeV. Thus, 6 MeV alpha particle can deliver much larger incident energy arriving the human cell sample. However, in term of total energy deposited per incoming particle in the cell sample, the results are similar on both cases due to the really tiny size of a Eukaryotic cell. 4 MeV alpha source has even higher energy deposition in the Eukaryotic cell sample. Overall, the  $7 \mu\text{m}$  CVDD membrane can work as a vacuum window for either 4 and 6 MeV alpha source to allow particles traverse and hit the cell sample for radiation biology research purpose.

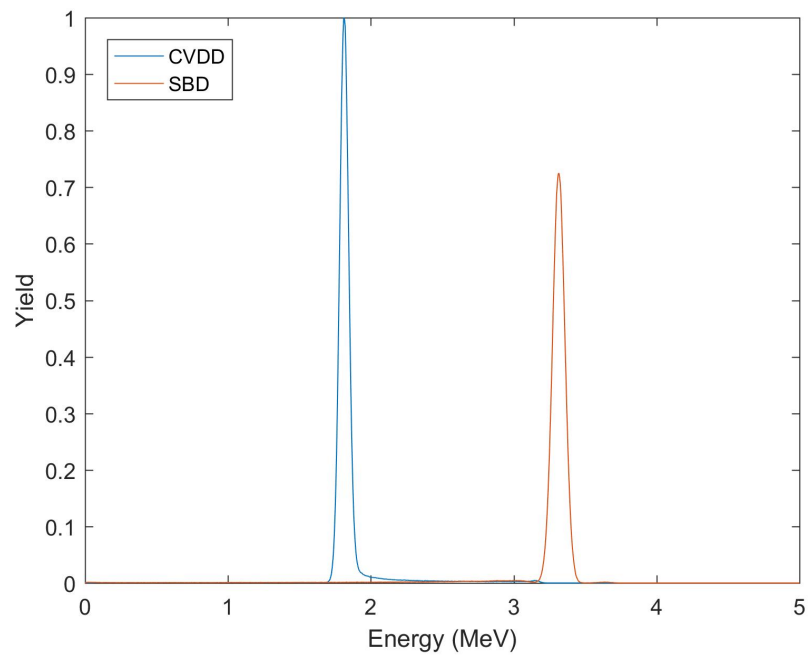
The pulse height spectrum of CVDD and SBD in the condition of  $\cos\theta$  distributed  $6 \mu\text{m}$  diameter 4 and 6 MeV alpha beam displays in Figure 5.5. Same normalization

described previously was applied to generate yield. For 4 MeV alpha beam (Figure 5.5a), the CVDD spectrum peaks at 2.70 MeV and SBD spectrum has a board peak with maximum yield at 0.33 MeV. From Figure 5.5b, the peak of CVDD locates at 1.81 MeV and the peak of SBD is at 3.32 MeV for 6 MeV source. The peak energy of CVDD is exactly the energy deposited by a source alpha particle in the diamond beam window because the alpha particles exit from vacuum so no energy loses before it goes through the CVDD window. This peak is narrow due to highly collimated source bombarding which is is distinct from Figure 5.4. The long tail of the peak shape suggests a Landau distribution which describes the energy straggling for a traversing heavy particle. 6 MeV alpha particles remain energetic after penetrate the diamond vacuum window and cell sample and deposit all the left energy into the silicon SBD forming a narrow strong peak while 4 MeV  $\alpha$  particle exhausts almost of its energy after cell sample absorption.

MCNP simulation of microbeam configuration proved the feasibility of installing an ultra-thin CVDD membrane working as both a vacuum beam window and a transmission-type detector. For either 4 or 6 MeV alpha beam generated by the 3 MV KN Van de Graaff accelerator, an alpha particle is sufficient to transport through the CVDD membrane and deposit energy into the Eukaryotic cell sample.



(a) 4 MeV alpha beam



(b) 6 MeV alpha beam

Figure 5.5: CVDD-SBD  $\Delta E$ -E MCNP pulse height spectrum on microbeam configuration for 4 and 6 MeV alpha beam

# Chapter 6

## Characteristics Investigation

In this chapter, the characteristics of the ultra-thin SCVD diamond detector for alpha particles were investigated. The  $\Delta E$ -E configuration involving the ScCVDD detector and a silicon surface barrier detector was used to verify the transmission capability of the ultra-thin diamond detector as an alpha counter.

### 6.1 Ultra-thin ScCVDD Detector Characterization

#### 6.1.1 Setup and Methodology

The experiments of investigate the characteristics of the ultra-thin ScCVDD detector were conducted by observing oscilloscope waveform and collecting pulse height spectrum of the ScCVDD detector irradiated by a sealed  $^{241}\text{Am}$  alpha disk source from Eckert & Ziegler Isotope Products with a calibrated activity of 4.514 kBq on 1st May, 2018. The ScCVDD detector consisting the etched ScCVD diamond sample and PCB was mounted in the aluminum chamber beneath an alpha source in a holder

made by Rexolite 1422 spacing by 0.58 mm thick washers. The NIM electronic chain setup used in the experiment is illustrated in Figure 6.1. A coaxial cable connected the ScCVDD detector to a CEAN A1422 charge sensitive preamplifier with gain of 45 mV/MeV. The detector was biasing by a HAMAMATSU C9525 desktop high power supply (voltage range from + 0 to 1000 V). The preamp output was fed to a CAN-BERRA 2024 shaping amplifier which had shaping time setting of 0.5  $\mu$ s and gain of 30 (coarse gain 30 and fine gain 1.0). A EG&G ORTEC SpectrumMaster 919 multi-channel buffer (MCB) including multi-channel analyzer (MCA) and analogy-digital converter (ADC) was used with MAESTRO V6.06 spectrum acquisition software in the PC to produce pulse height energy spectrum. An Agilent Technology DS01102B digital oscilloscope was connected to the preamplifier and shaping amplifier for signals observation.

Slowly applied high voltage to the ScCVDD detector. Observed signals from the oscilloscope and then collected MCA spectrum by MAESTRO on the PC. The data were analyzed and plotted by MATLAB.

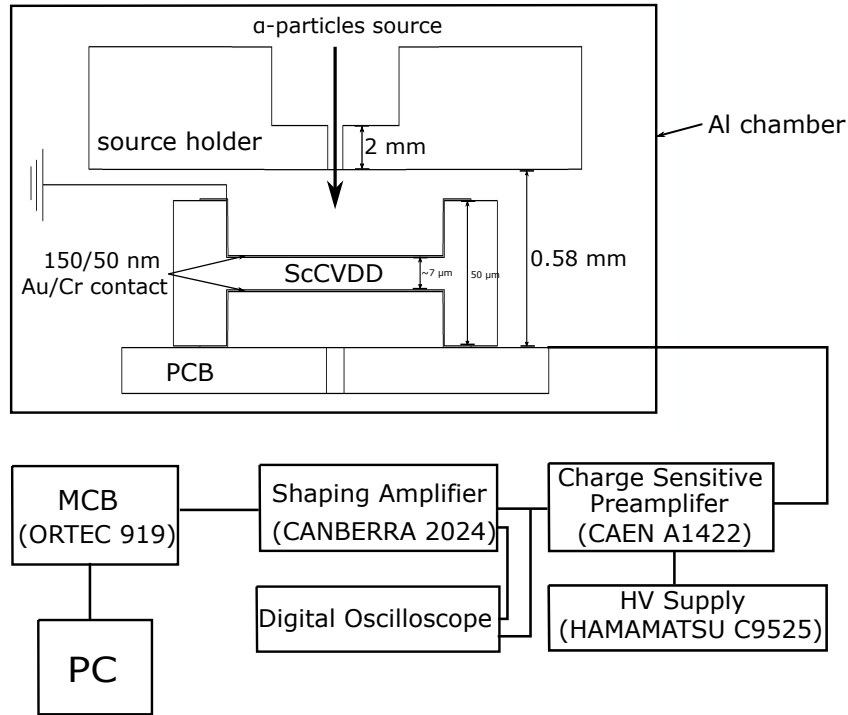


Figure 6.1: (a) Schematic of the ScCVDD detector and block diagram of the electronic chain. MCB stands for multi-channel buffer, PC stands for personal computer

### 6.1.2 Functionalities

Unlike silicon detectors could produce signal even with no bias due to small band gap for electrons excitation, the diamond detector requires high voltage to create strong electrical field in the bulk for electrons and hole drifting and signals generation. Unstable signals with strong fluctuation were observed from the oscilloscope for at 10 V biasing. When bias voltage was larger than 20 V, stable pulsing signals can be seen. A typical stable output shown on the oscilloscope is demonstrated in Figure 6.2 as an example. The upper line shows a 30 mV raise of preamp signal and the lower

one represents the shaping signal with 11 V pulse height. As bias voltage increases from 20 V to 100 V, the pulse height of the shaping preamp signal tends to stabilize at around 15 V. Note that the pulse amplitude displayed on this oscilloscope is 5 times its originals.



Figure 6.2: Preamp output (CH1, yellow) and shaping amp output signal (CH2, green) of the ScCVDD detector at 60 V. 5X amplitude magnification on oscilloscope display

Figure 6.3 is the MCA spectra of the ScCVDD detector under different bias voltages for 600 s collection. The shape of spectrum shifts as voltage increases and stabilizes at 80 V. The counting rate grows as voltage rises. The alpha peak becomes recognizable at 60 V and a clear peak forms at 80 and 100 V well apart from the low energy peak, which means the ultra-thin optical grade ScCVDD detector therefore

can be used as an alpha particle counter or even a spectroscopic detector. The optimal operation voltage should be no less than 80 V. 100 V bias was used for following experiments. For positive bias, holes are the major contributors of the signals.

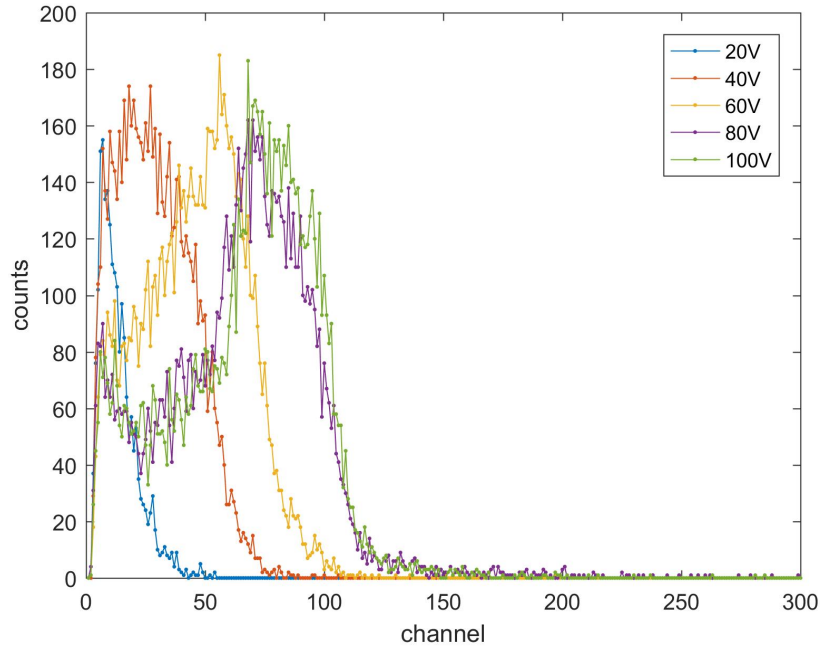


Figure 6.3: The pulse height spectra of the ScCVDD detector under different operation voltages. Channel cuts at 300. Collection time 600 seconds.

To investigate the counting and spectroscopy performance of the ultra-thin Sc-CVDD detector, the detector ran 1800 s for  $^{241}\text{Am}$  source to acquire higher counts. It was additionally tested with a  $^{244}\text{Cm}$  alpha disk source from Eckert & Ziegler Isotope Products with a calibrated activity of 3.699 kBq on 1st Aug, 2011 for 3000 s at 100 V bias. The spectrum was combined with the result of 1800 s irradiation of the  $^{241}\text{Am}$  source shown in Figure 6.4.

The counting rate for  $^{241}\text{Am}$  and  $^{244}\text{Cm}$  is 14.3 and 8.6 cps respectively while the activity of  $^{241}\text{Am}$  and  $^{244}\text{Cm}$  source at the experiment date is 4.5 and 2.6 kBq. The

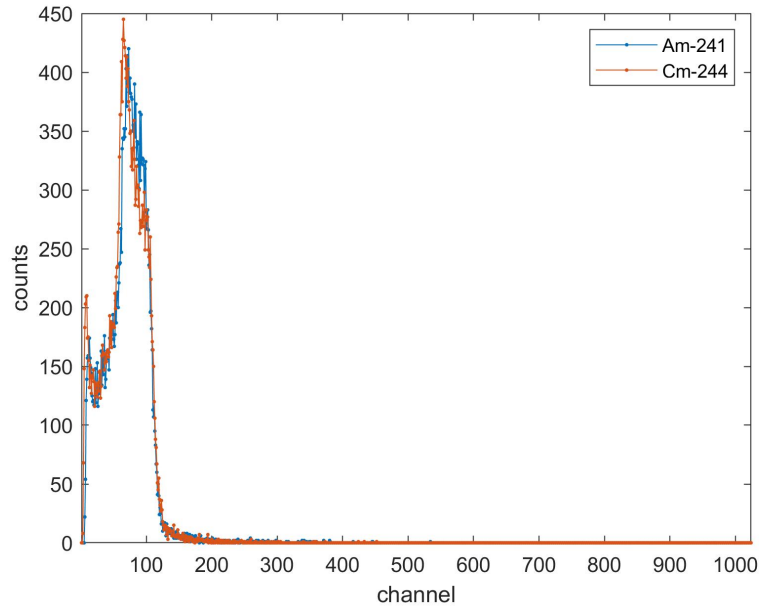
absolute total efficiency of the ultra-thin SCVDD detector is about 0.3 %. Consider the collimation, the intrinsic total efficiency is 16 % based on MCNP simulation that about 2 % of source particles are going to hit the diamond detector.

From Figure 6.4a, the general shape of two spectra are identical which contains an edge at very low channel and a main peak with maximum counts at around channel 70. The edge at low energy region is suspected as a gamma peak since  $^{241}\text{Am}$  and  $^{244}\text{Cm}$  both emit 0.05 MeV-ish of gamma radiation. The full energy peak shown in MCNP simulation result (Figure 5.4) is absent in the experiment which may be caused by weak contact or no electrode on the 50  $\mu\text{m}$  thick "highland" part of the diamond sample. The etched part provided the signal for our objective, so the missing full energy peak is not a concern.

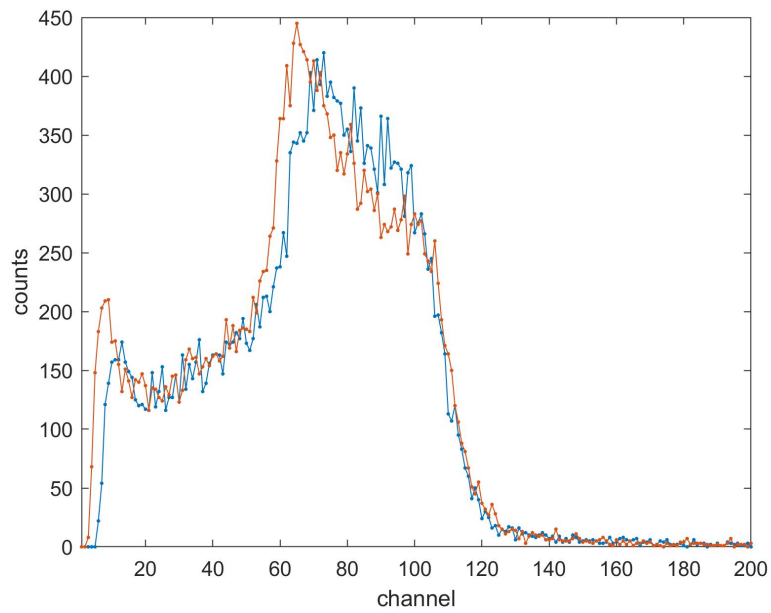
Figure 6.4b is a closed-up look of channel 0 to 200 to focus on the peaks. The very first tips located at channel 9 and 13 for  $^{244}\text{Cm}$  and  $^{241}\text{Am}$  spectrum respectively. The background noise test showed very clean MCA spectrum and the background signal has pulse height of 16 mV on the oscilloscope. For channel 10 on the MCA spectrum, the pulse height is about 100 mV which is significantly larger than the background tested by an ORTEC 419 pulser. Thus, the edges shown in the spectra are not electronic noise.  $^{244}\text{Cm}$  has major gamma at 0.043 MeV and  $^{241}\text{Am}$  has a main gamma decay at 0.059 MeV. For the ultra-thin ScCVDD with electrical field  $\sim 14\text{V}/\mu\text{m}$ , it has capability to detect gamma rays. The edge at low energy is considered as for gamma radiation. The gamma edge conjoins with the main peak, so cannot determine more spectroscopic information.

The second peak is considered as the alpha peak. An interesting downward sloping incline after the peaking point of the main peak could be seen. This may be caused

by the nonuniform thickness of the etched diamond sample due to imperfect overlaps from double-side etching. Theoretically, the energy spectrum of ionized particles traversing thin films obeys the Landau-Vavilov distribution instead of the Gaussian distribution [86]. However, the peak obtained in the experiment could not be simply fitted by the Landau probability density function, which may imply a complex energy straggling within the nonuniform thick diamond membrane due to imperfect overlapped double-side etching circles. More study is needed for peak fitting, but it is not the focus of scope of this work. For asymmetric peak, the most probably energy is its maximum. The peak channel with maximum count of  $^{244}\text{Cm}$  is at 65 while  $^{241}\text{Am}$  peaks at channel 73.  $^{244}\text{Cm}$  has major alpha energy of 5.80 MeV and  $^{241}\text{Am}$  emits 5.48 MeV alpha particles. Due to higher incident energy, the peak location of  $^{244}\text{Cm}$  would be expected to on the left of  $^{241}\text{Am}$  peak, which is what shows in the experimental result. Nevertheless, two peaks are not well enough distinguishable as only the maximum points are separated by a few channels which may be just caused by fluctuations. Additionally, the full width at half maximum (FWHM) is approximately 50 channel which results a 0.7 peak resolution. Overall, the fabricated ultra-thin ScCVDD detector is limited capable for spectroscopic measurement of alpha particles with poor resolution. Spectroscopy grade ScCVDD detector may require more effort on fabrications.



(a)



(b)

Figure 6.4: (a) The pulse height spectra of the ScCVDD detector for 1800 s  $^{241}\text{Am}$  source and 3000s  $^{244}\text{Cm}$  source irradiation respectively (b) Close up of (a) from channel 0 to 200

### 6.1.3 Trapping Phenomenon and Restoration

The impurities and defects of the diamond crystal can cause trapping of the charge carriers and consequently the distortion of the signals. Trapping is a common issue especially for diamond charge particles detector. Figure 6.5 shows an example of the pulse height spectrum degradation of the ultra-thin ScCVDD detector at 100 V. Compare it with normal spectra displayed previously (Figure 6.4), a high peak differentiates at around channel 100 formed the third peak in the spectrum. The trapping phenomenon had not been found at beginning of the experiment until about one month after. A possible reason for the trapping may be the alpha radiation induced defects of the diamond crystal. These defects create trapping center holding electrons or holes. In this case, the localized internal electrical field builds up which is referred as polarization effect. In addition, the optical grade ScCVDD contains more nitrogen impurities which may become deep trapping centers. When biasing applied, external electrical field dominated, the trapped charge carriers may be released and generate extra signals.

A long-time continuous measurement was conducted. MEASTRO v6.06 spectrum software can repeat the spectrum collection operation via script commands. Spectra were automatically collected every 10 mins for 10.3 hours at 100 V bias irradiated by  $^{241}\text{Am}$ . The results indicated that spectrum with trapping phenomenon can be restored to normal by applying high voltage for one to two hours. Figure 6.6a illustrates the spectrum collected at time 30, 60, 90 and 120 mins. The trapping phenomenon was obvious during the first 60 mins data and then the deteriorated spectrum was gradually restoring. The extra peak became smaller at 90 mins and the spectrum was backing to the non-trapping status. At 120 mins, the extra peak disappeared totally.

The counting rate of each 10 mins data collection was plotted as Figure 6.6b. The counting rates were high at beginning since the trapping creating an extra peak that falsely increased the total number of counts. As trappings was restoring by biasing over time, the counting rates declined and reached the cave at 100 mins as restoration completed. Once trapping was gone, the counting rates started increasing in a trend the fitting line indicated and the peaks located at channel  $70 \pm 15$ . The rising counting rate may suggest the priming effect that the collection efficiency increases as prolongation of irradiation time.

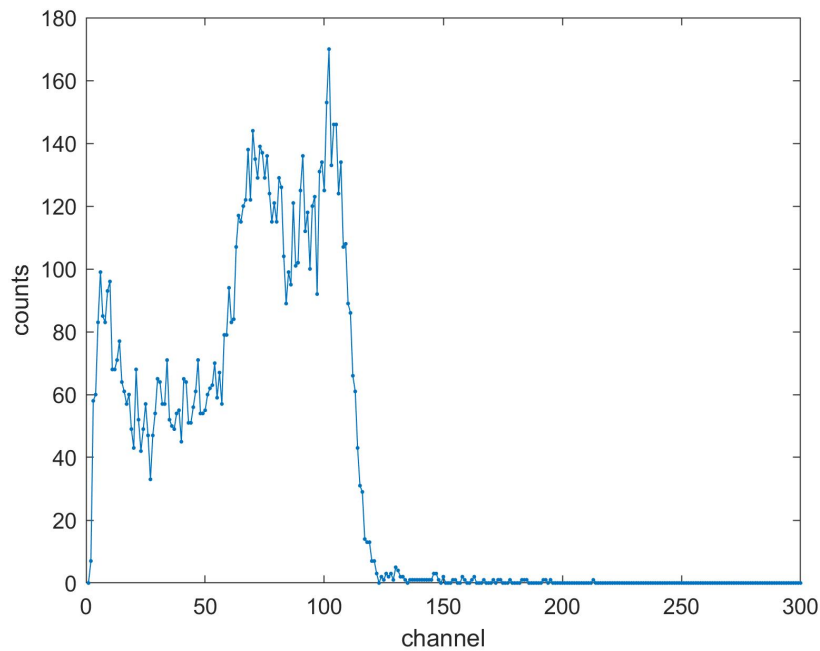
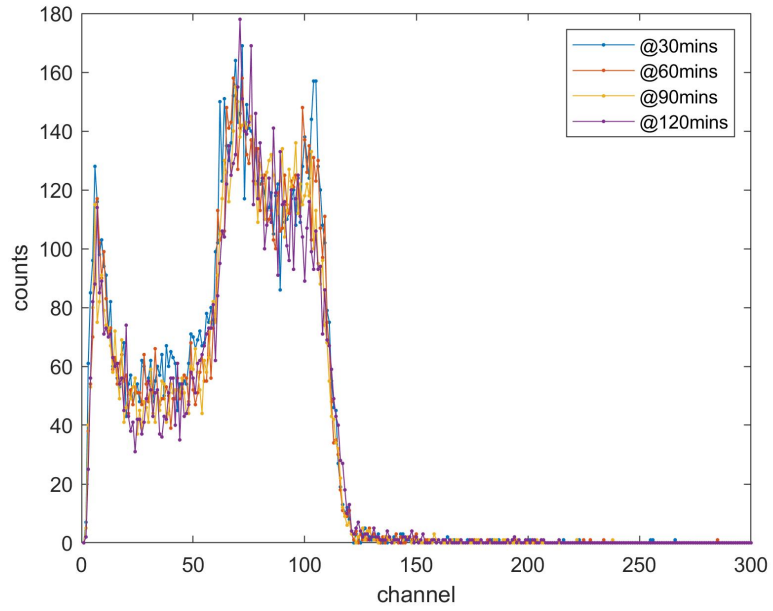
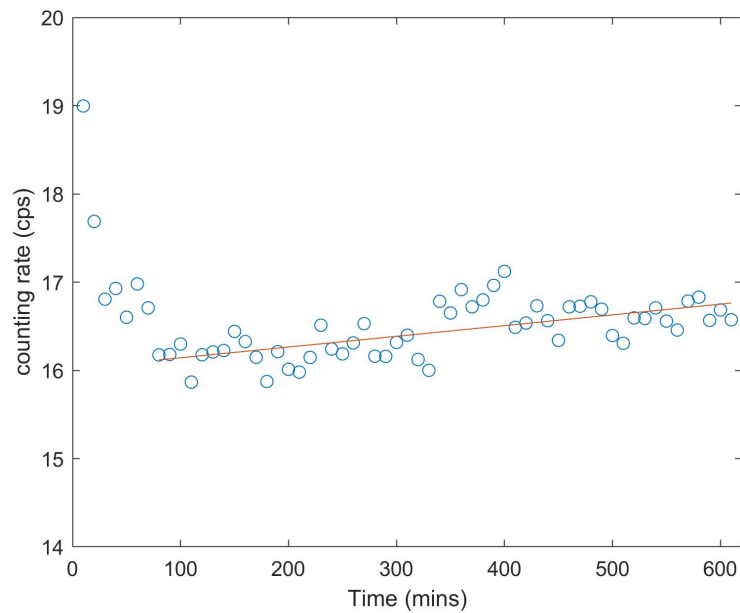


Figure 6.5: A pulse height spectrum of the ScCVDD detector for 600 s  $^{241}\text{Am}$  source demonstrating the trapping phenomenon



(a)



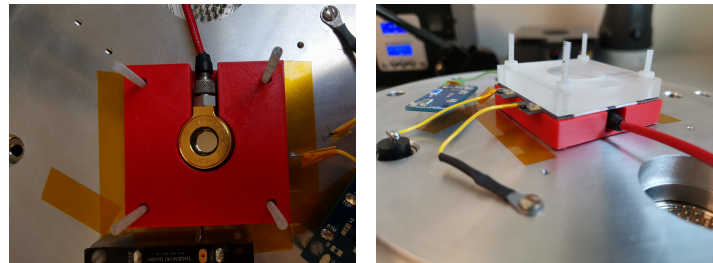
(b)

Figure 6.6: (a) ScCVDD detector MCA spectra at 30, 60, 90 and 120 mins of the 10.3 hours data acquisition (b) The counting rate of each 10-min measurement over 10.3 hours, red line is the linear fit of the data point from 90 mins

## 6.2 ScCVDD-SBD $\Delta E$ -E System

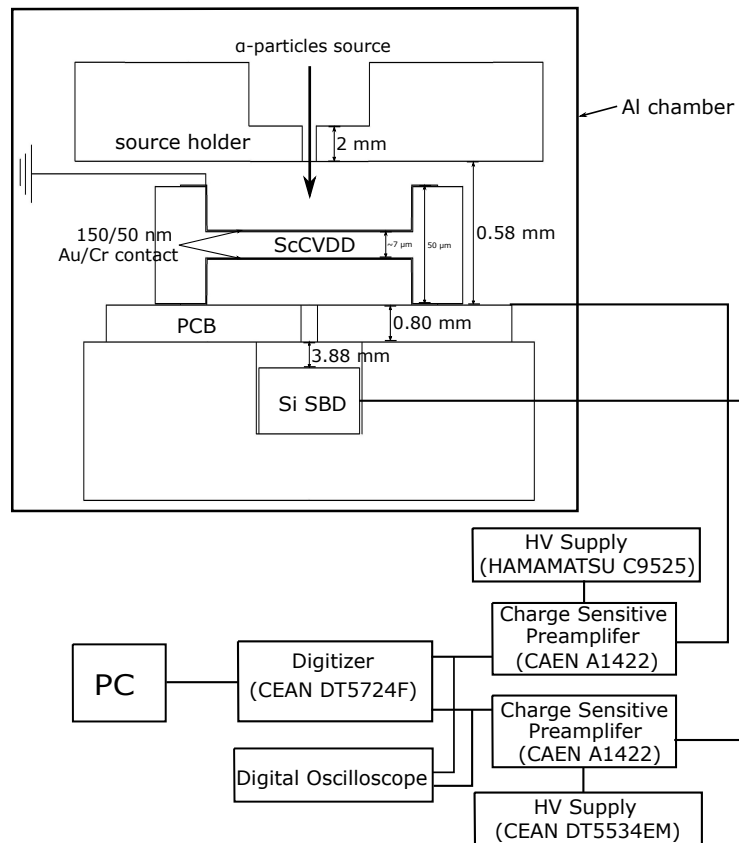
### 6.2.1 Setup and Methodology

A  $\Delta E$ -E system, as the name suggests, has a radiation transmissive  $\Delta E$  detector and a E detector for full energy deposition to discovery the energy loss in  $\Delta E$  detector for transmission ability verification. In this work, an Ortec AMETEK silicon surface barrier detector (SBD) TD-015-050-100 was selected as the E detector placed after the the Ultra-thin ScCVDD detector ( $\Delta E$  detector). The silicon detector TD-015-050-100 is a planar totally depleted N-type silicon SBD with 50 mm<sup>2</sup> active area and 100  $\mu\text{m}$  depletion depth. The silicon wafer is arranged in a mount with a microdot connector. Figure 6.7a shows the SBD holing by a PLA plastic holder 3D printed at McMaster Lyons New Media Centre. The overall arrangement is illustrated by Figure 6.7b that the <sup>241</sup>Am source, ScCVDD detector and SBD are in a sandwich-like configuration. Figure 6.7c demonstrates the  $\Delta E$  system in the chamber and electronics chain for  $\Delta E$ -E experiment. The 3.88 mm gap indicates the distance from the silicon wafer of SBD to the bottom of the PCB. The ScCVDD detector was fed to a CEAN A1422 charge sensitive preamplifier powered at 100 V. The SBD was fed to another identical CEAN A1422 preamplifier biased by a CEAN DT5534EM power supply at 35 V. Both preamp outputs connected to a CEAN DT5724F 4-channel 14-bits desktop digitizer. A PC was connected to the digitizer to collect data via CoMPASS data acquisition software with pulse height analysis (PHA) firmware. A Tektronix TDS 210 digital oscilloscope was used to monitor the preamp signals of two detectors.



(a)

(b)



(c)

Figure 6.7: (a) Photo of the SBD placing in the holder (b) Photo of the source holder-ScCVDD detector-SBD configuration (c) Schematic of the  $\Delta E$ -E system and block diagram of the electronic chain. PC stands for personal computer

Remarkably different from Section 6.1, the instruments used for  $\Delta E$ -E measurements changed from NIM analogy system to desktop digital system to take advantages of the CEAN digital system for recording time information outputted as list mode for offline coincidence operation. For the digital system, some key parameters was adjusted according to CoMPASS Quick Start Guide [87] in order to acquire data properly. By observing the waveform displayed on the CoMPASS signal inspector interface, the discriminator threshold was adjusted above the baseline noise to filter unwanted signals out. The input rise time was set to match the height of the RC-CR<sup>2</sup> signal to avoid over- or under-estimated counting. Trigger hold-off duration was set to long enough to cover the RC-CR<sup>2</sup> signal. Trapezoid filter is the core of digital shaping. The suitable trapezoid rise time is corresponding to about 2 or 2.5 times of analogy shaping time. The trapezoid rise time was set to 1.25  $\mu\text{s}$  for the diamond detector and 2  $\mu\text{s}$  for the SBD. The flat top was set to 1.5 and 1  $\mu\text{s}$  for ScCVDD and silicon detector respectively. The energy fine gain was 10. The CoMPASS configuration parameters in details are summarized in Table 6.1, where LSB stands for least significant bits. To avoid the trapping phenomenon, the ultra-thin ScCVDD detector need to be biasing in advance at 100 V for at least 90 mins to eliminate trapping before the  $\Delta E$ -E measurement.

The list mode data produced by CoMPASS has three columns: the first column is time stamp of the signal processing by the digitizer in unit of ps, the second column is the energy or channel number of the event and the third column contains flags which represent additional information of the event. By analyzing list mode data, a coincidence time window can be determined. In the coincidence operation, only the event within the coincidence time window present in both diamond and silicon

detector is going to be kept and other events will be discarded. Pulse height spectrum can be reconstructed from the list mode data by plotting the histogram of channels. The offline analysis was done by MATLAB.

Parameters	ScCVDD	SBD
input polarity	+	+
DC offset	10%	10%
Input dynamic	2.25 V <sub>pp</sub>	2.25 V <sub>pp</sub>
Threshold	29 LSB	20 LSB
Trigger hold-off	180 ns	150 ns
Input rise time	200 ns	150 ns
Trapezoid rise time	1.25 $\mu$ s	2 $\mu$ s
Trapezoid flat top	1.5 $\mu$ s	1 $\mu$ s
Numbers peaking	4	16
Energy fine gain	10	10
Energy number channels	1024	1024

Table 6.1: CoMPASS acquisition parameters for the ScCVDD detector and SBD

### 6.2.2 Coincidence Time Window

An alpha particle emitting from the source penetrates through the ScCVDD detector and deposit all the energy left into the SBD. In this process, both detectors are triggered subsequently so a time difference can be observed. The time interval between events was calculated by finding the minimum time difference between events from two detectors time stamps.

Figure 6.8 is a histogram of the time interval between events by analyzing the

$\Delta E$ -E list mode data for 300 s irradiated by  $^{241}\text{Am}$  source. The histogram indicates all events happened within  $0.22\ \mu\text{s}$  and the most major events distribute at  $0.1$  to  $0.14\ \mu\text{s}$ . Thus, a coincidence time window of  $0.22\ \mu\text{s}$  can be chosen. If the diamond and silicon detector have events taking place within  $0.22\ \mu\text{s}$ , it would be considered as a coincident event. A notable fact found from the list mode time data was the signal of silicon SBD arriving the digitizer earlier than the ScCVDD detector, even although alpha particles traverse the diamond detector first. Diamond should be able to deliver fast signals due to high carrier mobility. The reason of the lag in the experiment may be because of poor signal transmission caused by large overall capacitance due to extremely small thickness. The electronic connection made via flat copper wire having relatively large resistivity that may cause poor signal readout performance.

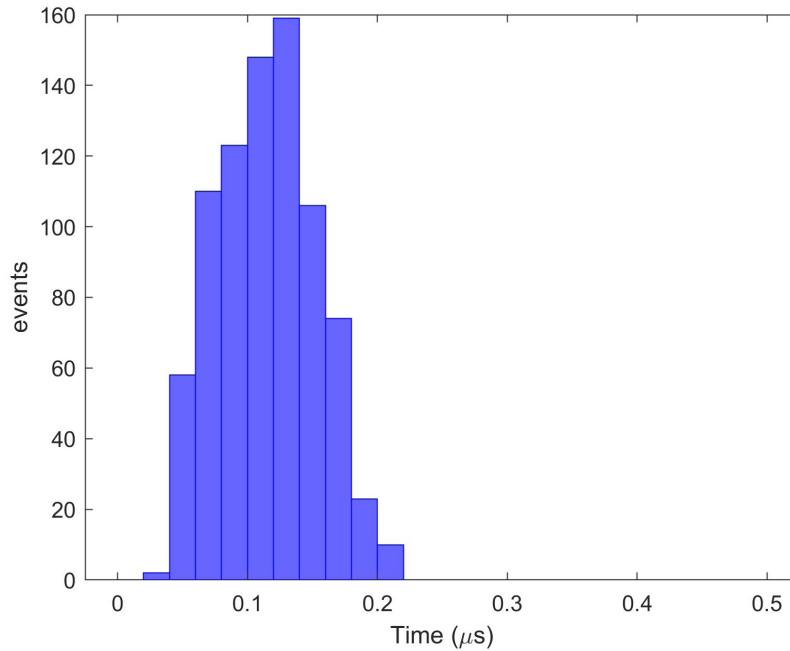


Figure 6.8: Time intervals between events for  $^{241}\text{Am}$  300 s

### 6.2.3 $\Delta E$ -E Measurements

When two detectors worked at the same time, the waveform signal observed from the oscilloscope triggering by the silicon detector shows in Figure 6.9. The upper wave is the preamp output of the ScCVDD detector and the bottom signal is from SBD. The pulse height of the ScCVDD and SBD is about 6 and 24 mV respectively. Since the identical preamplifiers were used, it indicates approximately 4 times more amount of charges generating in the silicon detector compared to the diamond detector, which implies the diamond needs about 4 times more energy to produce charge carriers. In fact, the energy required for electron-hole pair creation for silicon and diamond is reported as 3.62 and 13.2 eV [37, 71] giving a ratio of 3.6.

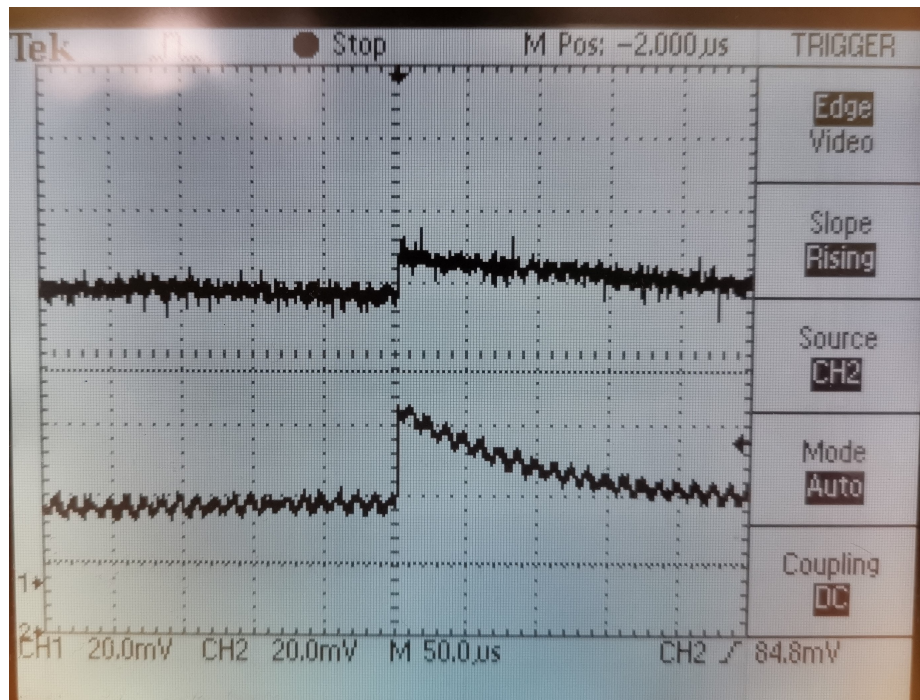


Figure 6.9: Preamp output of ScCVDD detector (upper) and SBD (lower). Signal is triggered by SBD. 1X amplitude

The original  $\Delta E$ -E measurement of the ScCVDD and SBD spectrum for 3600

s is illustrated in Figure 6.10. Apparently, as seen from the spectra, the ScCVDD detector has much more counts than the SBD and the counting rate for ScCVDD and SBD is 14.4 and 3.06 cps respectively. The counting rate of ScCVDD detector is very close to the analogy setup in previous section as expected. The peak shape is somehow different from typical spectra acquired by ORTEC MCB where a edge is at low energy region. The gamma edge was filtered out by the threshold setting in CEAN digital system. The experimental result of counting rate ratio is 21.3% which is comparable to the MCNP simulation result in section 5.2.3 that about 27.3% of particles entering the diamond can reach the silicon detector eventually. The PCB hole works as a collimator filtering out part of traversing particles. Another interesting feature of the spectra is the board peak of the silicon SBD. The SBD peak doesn't have a sharp peaking edge as simulated in Figure 5.4 which could probably because of the inhomogeneous energy of traversing particles since the thickness of the ultra-thin ScCVDD is not uniform caused by double-side etching.

By applying coincidence operation, only events on the SBD and also on ScVDD detector within  $0.22 \mu\text{s}$  time window mark as coincident counts while other events are filtered out. The coincidence spectrum of the ScCVDD and SBD shows in Figure 6.11a and 6.11b respectively. The total coincidence counts of the diamond detector is reduced significantly to 18.8% of the original. The coincidence spectrum of the SBD has 11.4% counts reduction. In principle, the SBD spectrum should remain no change since all events produced in SBD should also be found on the diamond detector. However, there are some events recorded by SBD but no corresponding events on the ScCVDD detector. An explanation is the trapping effect caused disruption on charge collection and loss of events. An possible evidence of charge carriers trapping is a spike

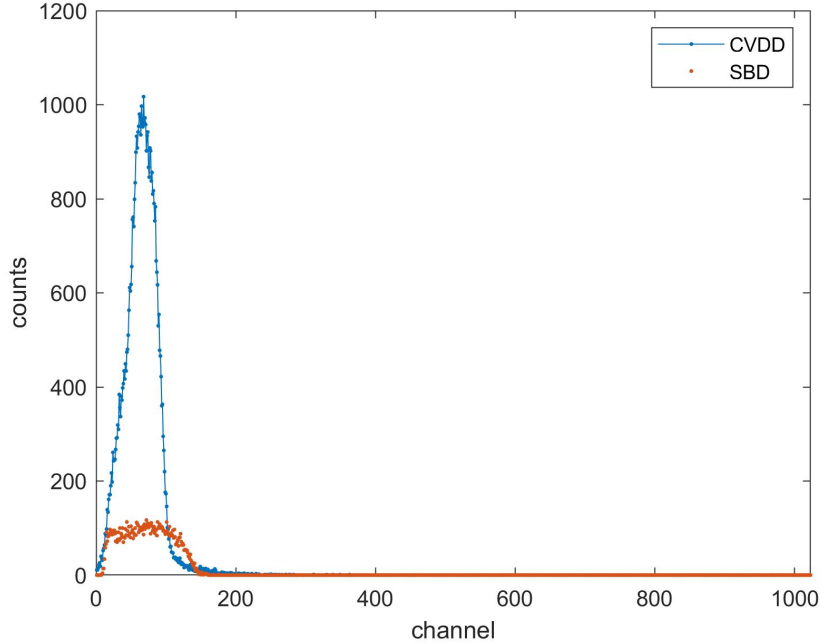
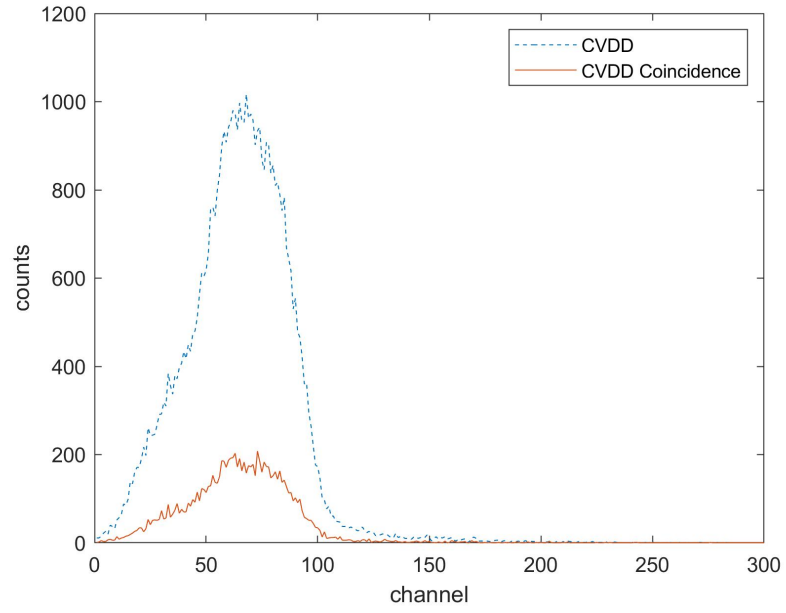
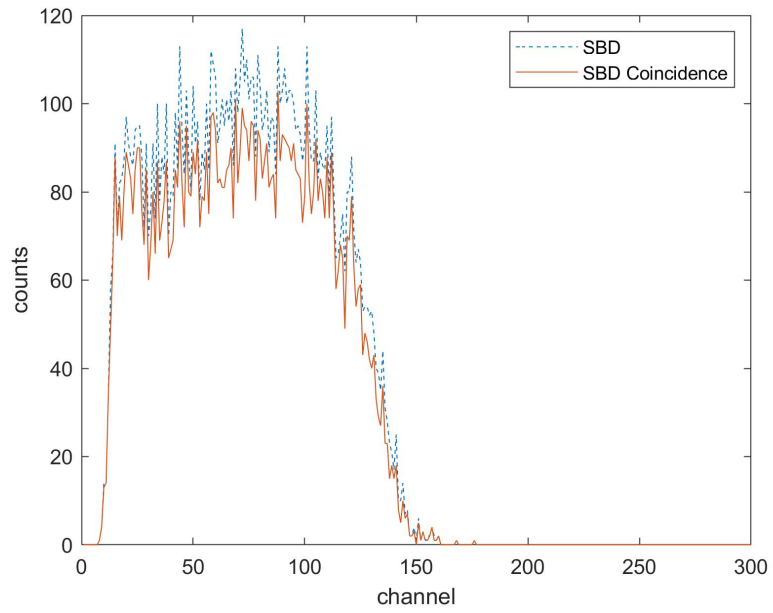


Figure 6.10: The original  $\Delta E$ - $E$  spectra of the ScCVDD detector and SBD

in the peak of the coincidence ScCVDD spectrum. Even though the diamond detector had been biased in advance, it may not eliminate all the trapped carriers and trapping may re-accumulate during the experiment. The result implies it is difficult to achieve a perfect in-and-out equilibrium of trapped carriers in practice. The coincidence  $\Delta E$ - $E$  spectra combining Figure 6.11a and 6.11b is displayed in Figure 6.11c. Two peaks are overlapped with each other from channel 0 to 150. The  $\Delta E$ - $E$  experiment successfully proves the transmission of the ultra-thin ScCVDD detector.



(a)



(b)

*continue to next page*

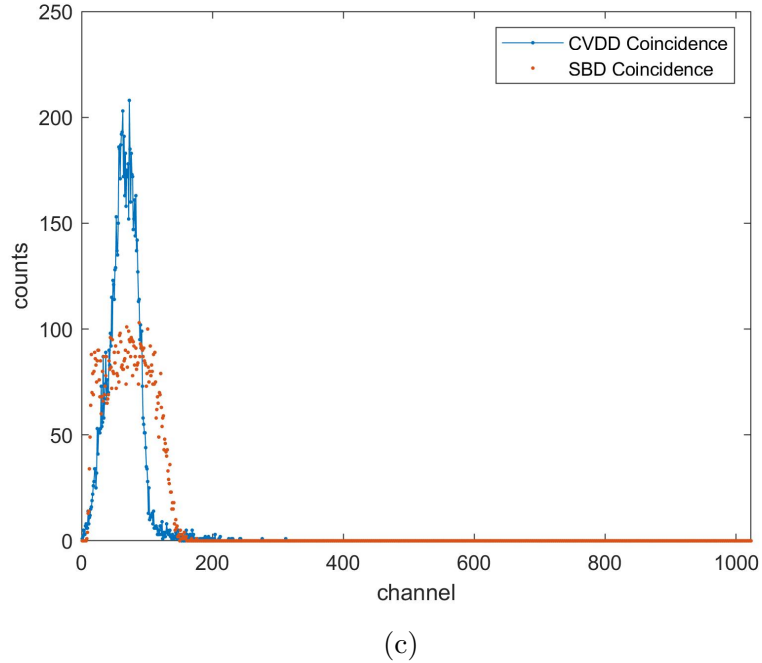
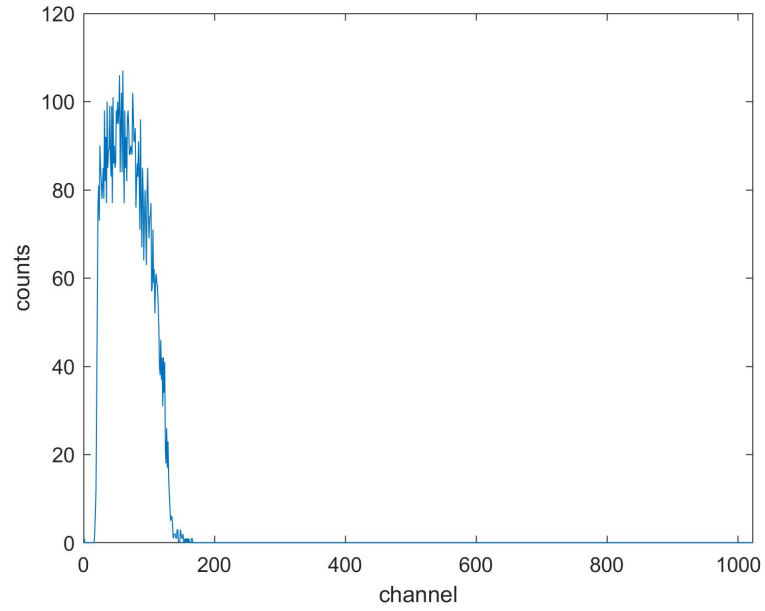


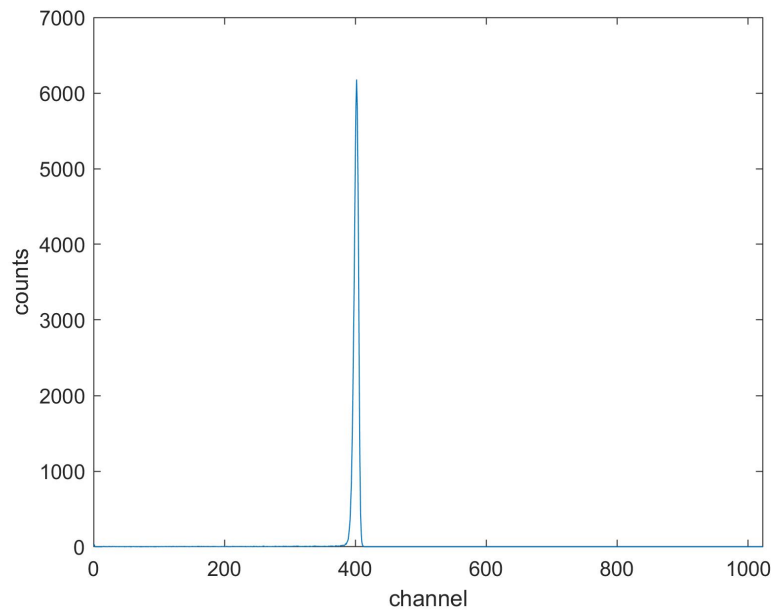
Figure 6.11: (a) The spectra of ScCVDD detector with and without coincidence, channel cuts at 300 (b) The spectra of SBD with and without coincidence, channel cuts at 300 (c) The  $\Delta E$ -E coincidence spectra of the ScCVDD detector and SBD

#### 6.2.4 ScCVDD Thickness Reassessment

The  $\Delta E$ -E system can be used to estimate the thickness of the  $\Delta E$  detector by spectrometry analysis. The setup kept the same electronics chain as described in Section 6.2.1. Collected SBD energy spectrum only for 3600 s irradiation of  $^{241}\text{Am}$  source with the ScCVDD detector in the way. Then replaced the ScCVDD detector by an empty PCB with no diamond membrane installed and collected SBD spectrum with no diamond in the way for another 3600 to acquire statistically enough counts. The energy spectrum of the SBD with and without the ultra-thin ScCVDD in the way shows in Figure 6.12.



(a)



(b)

Figure 6.12: (a) Spectrum for SBD with the ScCVDD detector in the way (b) Spectrum for SBD only with an empty PCB in the way. Acquisition time 3600 s

In Figure 6.12b, the peak locates at channel 402 calculated from Gaussian fitting. In this case, nothing but air is between the silicon detector and the  $^{241}\text{Am}$  source. The air gap is  $2+0.58+0.8+3.88=7.26$  mm referred to the setup (Figure 6.7). The incident energy of 5.48 MeV  $^{241}\text{Am}$  alpha particles upon the SBD is calculated by SRIM code using the method described in Section 5.1.1. The compounds of air use SRIM build-in ICRU 104 dry air with density  $1.63\times 10^{-3}$  g/cm<sup>3</sup>. The calculation also takes account the the energy loss of alpha particles in 100 nm Au electrode of the SBD. The result shows the 5.48 MeV alpha particles lose 0.835 MeV energy in air and 0.046 MeV energy in Au contact. The peak is corresponding to the energy deposition of 4.599 MeV alpha particles. The channel number can be converted into energy by calibrating channel 402 for 4.598 MeV.

The peak in Figure 6.12a could not be nicely fitted by a Gaussian function so an estimation was made. The peak has maximum counts at channel 60 corresponding to 0.686 MeV. The board spreading from channel 23 to 97 as the uncertainty of the mean corresponds to 0.263 to 1.109 MeV. Compared with the MCNP simulation for 7  $\mu\text{m}$  diamond membrane in Figure 5.4, the actual thickness of the ultra-thin ScCVDD in the experiment is definitely larger than 7  $\mu\text{m}$ . The actual thickness can be calculated by assuming the incident energy of alpha particles onto the SBD is 0.686 MeV with diamond membrane in the way by the method used previously with modifications. The ScCVDD detector is between the source and SBD with air presenting so the computation could not be done by simply calculating the thickness directly from Equation 5.1.3 since the initial and final energy for the diamond membrane is not certain without knowing the energy loss of alpha particles in the air gap between the source and the diamond detector. An initial guess for the thickness of the diamond

was set to 10  $\mu\text{m}$  to start the calculation. The energy of a 5.48 MeV alpha particle going through the air gap, 150/50 nm Au/Cr electrode, diamond, then bottom Au/Cr electrode, another air gap and finally depositing in the SBD is calculated to compare with the experimental value of 0.686 MeV. If the computed incident energy on the SBD is not equal to the peak energy, prompt another guess to restart the calculation. The iteration occurs several rounds and the diamond mean thickness 8.315  $\mu\text{m}$  is calculated with uncertainty of 0.690  $\mu\text{m}$  from the spread of energy peaks.

The mean thickness of the ultra-thin ScCVDD is 8.315  $\mu\text{m}$  based on  $\Delta E$  spectrometry, which is larger than the average thickness measured by stylus profilometer and Alicona InfiniteFocus G5. As mention in Section 4.2, the double-side etching brought nonuniform thickness, imperfect flatness and significant uncertainty for the measurement. Although the thickness may vary only by about 1.3  $\mu\text{m}$ , the energy loss increased remarkably due to the poor penetration ability of alpha particles in the diamond. With  $8.315 \pm 0.690$   $\mu\text{m}$  thickness, the electrical field applied on the ScCVDD detector on 100 V bias is  $12 \pm 1$  V/ $\mu\text{m}$ .

# Chapter 7

## Conclusion and Future Work

### 7.1 Conclusion

In order to precisely quantify the number alpha particles extracted from the accelerator hitting the biologic cell sample, an alpha-particle counter is required. Thanks to the CVD technology, CVD diamond, especially single crystalline CVD diamond, inherits the superior intrinsic characteristics, such as supreme hardness, excellent mechanical property and high thermal conductivity, with controllable impurity concentration and affordable costs. The striking electronic properties including wide band-gap, high carrier mobility and excellent thermal conductivity promises tremendous potential for diamond as a radiation detector. The ultra-thin single crystal CVD diamond membrane had been selected as an external charged particle sensitive transmission-type counter in a pre-cell configuration and also the beamline vacuum window for McMaster University Microbeam Facility. Due to the wide band gap characteristic of diamond, diamond detector is naturally visible light-blind which allows real time observation during the irradiation using optical microscopy and no

need for light-proof dark cage commonly used for thin plastic scintillator counter. The self-support mechanical property makes it possible to be installed as a beamline extraction vacuum window which avoids the scattering brought by an extra detector.

The ultra-thin ScCVDD detector made in this work started from a 50  $\mu\text{m}$  commercial ScCVD diamond sample. The fabrication processes involved were plasma etching, cleaning, metal contact deposition and post-metallization annealing. To assess the energy loss of alpha particles in electrodes and diamond, SRIM code was utilized to compute based on mass stopping power data. MCNP6 simulation was performed to study the energy deposition in material and predict pulse height spectrum for ScCVDD-Silicon  $\Delta\text{E-E}$  configuration. The feasibility of ultra-thin diamond as the vacuum window and counter in microbeam configuration was also studied.

The experiment of the ultra-thin ScCVDD detector characterization demonstrated the voltage-dependence of the pulse height spectra. The counting and spectroscopic properties of the ScCVDD detector were investigated. The counting rate for the  $^{241}\text{Am}$  source is 14 cps with intrinsic total efficiency about 16 %. Gamma and alpha peaks were identified from the spectrum with relatively poor peak resolution. Trapping phenomenon that deteriorated the spectrum was observed during the detector operation and it can be restored by continuously high voltage biasing. A  $\Delta\text{E-E}$  setup was built by adding a SBD beneath the diamond detector and list mode data containing time stamps was collected using a digital system. The coincidence operation verified the particles transmission through the ultra-thin ScCVDD to the SBD within 2.2  $\mu\text{s}$  time window. Based on  $\Delta\text{E-E}$  spectrometry, the thickness of the ultra-thin diamond sample was reassessed to be  $8.315 \pm 0.690 \mu\text{m}$ . A major problem raised from the experiment was the nonuniform thickness due to imperfect overlapped

double-side etching caused by accidentally flipper-over during the second around of plasma etching.

## 7.2 Future work

The thickness of the ScCVD diamond membrane can decrease down to about 5  $\mu\text{m}$  by plasma etching to further reduce the energy loss of alpha particles in the diamond. Electronic grade ScCVDD membrane with less impurity concentration could be chosen for spectroscopic characterization.

To achieve higher surface quality, the plasma etch should be done at once to avoid possible double-side etching to avoid the problem raised from double-side etching presented in this work. The nonuniform etched surface is an avoidable issue due to the nature of RIE, the surface quality of the etched diamond sample could be evaluated by scanning electron microscope (SEM) or Atomic force microscopy (AFM). The thickness measurement of diamond was suffered from serious profile fluctuation due to difficulties on optical focusing on nonuniform diamond surface. A better alternative way to measure the thickness is ion-beam-induced charge (IBIC) imaging. IBIC imaging is to use a scanning focused ion beam as probes mapping on the tested sample to measure and image the transport properties of semiconductor materials and devices [88]. The principle of measuring thickness by IBIC imaging is similar to the thickness reassessment Section 6.2.4 that calculates the thickness from energy loss at each pixel. IBIC technique could provide precise measurement on the variation of the thickness and also determine the transport properties at the same time.

An improvement regarding the electrode is to from Schottky contact on one side of the diamond and Ohmic contact on the other side [80] instead of currently 150/50 nm

Au/Cr on both side of the diamond. The Schottky contact side is used for grounding to take the advantage of the rectifying feature while the Ohmic contact provides unaffected charge carrier transfer for signal collection. For such a thin diamond plate, the signal transmission is a challenge issue due to large capacitance. The electronic connection between the diamond electrode to the PCB can be done by wire bonding to improve the signal readout of the diamond detector. The PCB location can be placed further away from the bottom of the aluminum base to achieve better grounding. The hole in the PCB acts like a collimator in  $\Delta E$ -E measurement, a redesign of the PCB layout is recommended.

The experiments done in this work were all in ambient environment. To reduce the energy loss of alpha particles in the air, the chamber should be vacuumed. The  $\Delta E$ -E data measured in vacuum can be used for the charge collection efficiency calculation. A 72-hour stability test should be performed to check the restoration of trapping phenomenon in long-time operation. Some important electronic properties investigation should be proceeded in the future to fully characterize the diamond detector. Current-Voltage (I-V) relationship needs to be measured by high precision electrometer for discovery the leakage current, Ohmic/Schottky behavior and breakdown voltage. The charge carrier drift velocity and mobility can be determined via transient current technique.

Once the ultra-thin ScCVDD detector is fully characterized, it can be glued on a screw cap and installed on the beamline as a beamline extraction vacuum window. The engineering and technique challenges of the installation need to be solved and the on-line performance of the ultra-thin ScCVDD detector for the radiobiology experiment can be tested.

# Bibliography

- [1] Sergej Tschachotin. Die mikroskopische strahlen-stichmethode eine zelloperationsmethode. *Biol. Zentralblatt*, 32:623–630, 1912.
- [2] Michael W Berns. Microbeams. In *Laser applications in medicine and biology*, pages 1–40. Springer, 1974.
- [3] Raymond E Zirkle and William Bloom. Irradiation of parts of individual cells. *Science*, 117(3045):487–493, 1953.
- [4] CL Smith. Microbeam and partial cell irradiation. In *International review of cytology*, volume 16, pages 133–153. Elsevier, 1964.
- [5] Frank Watt and Geoff W Grime. Principles and applications of high-energy ion microbeams. 1987.
- [6] Mark P Little, Richard Wakeford, E Janet Tawn, Simon D Bouffler, and Amy Berrington de Gonzalez. Risks associated with low doses and low dose rates of ionizing radiation: why linearity may be (almost) the best we can do. *Radiology*, 251(1):6–12, 2009.
- [7] Ramesh C Gupta. *Handbook of toxicology of chemical warfare agents*. Academic Press, 2015.

- [8] Silvia Gerardi. A comparative review of charged particle microbeam facilities. *Radiation Protection Dosimetry*, 122(1-4):285–291, 2006. ISSN 01448420. doi: 10.1093/rpd/ncl444.
- [9] Gerhard Randers-Pehrson, Charles R. Geard, Gary Johnson, Carl D. Elliston, and David J. Brenner. The Columbia University Single-Ion Microbeam. *Radiation Research*, 156(2):210–214, 2001. ISSN 0033-7587. doi: 10.1667/0033-7587(2001)156[0210:tcusim]2.0.co;2.
- [10] LA Braby. Microbeam studies of the sensitivity of structures within living cells. *Scanning microscopy*, 6(1):167–74, 1992.
- [11] M Folkard, KM Prise, B Vojnovic, HC Newman, MJ Roper, KJ Hollis, and BD Michael. Conventional and microbeam studies using low energy charged particles relevant to risk assessment and the mechanisms of radiation action. *Radiation Protection Dosimetry*, 61(1-3):215–218, 1995.
- [12] CR Geard, DJ Brenner, G Randers-Pehrson, and SA Marino. Single-particle irradiation of mammalian cells at the radiological research accelerator facility: induction of chromosomal changes. *Nuclear Instruments and Methods in Physics Research Section B: Beam Interactions with Materials and Atoms*, 54(1-3):411–416, 1991.
- [13] M. Folkard, B. Vojnovic, K. M. Prise, A. G. Bowey, R. J. Locke, G. Schettino, and B. D. Michael. A charged-particle microbeam: I. Development of an experimental system for targeting cells individually with counted particles. *International Journal of Radiation Biology*, 72(4):375–385, 1997. ISSN 09553002. doi: 10.1080/095530097143158.

- [14] Klaus-d Greif, Hein J Brede, Dieter Frankenberg, and Ulrich Giesen. The PTB single ion microbeam for irradiation of living cells. 217:505–512, 2004. doi: 10.1016/j.nimb.2003.11.082.
- [15] A Hauptner, S Dietzel, GA Drexler, P Reichart, R Krücken, T Cremer, AA Friedl, and G Dollinger. Microirradiation of cells with energetic heavy ions. *Radiation and environmental biophysics*, 42(4):237–245, 2004.
- [16] Alexander D. Dymnikov, David J. Brenner, Gary Johnson, and Gerhard Randers-Pehrson. Theoretical study of short electrostatic lens for the Columbia ion microprobe. *Review of Scientific Instruments*, 71(4):1646–1650, 2000. ISSN 00346748. doi: 10.1063/1.1150512.
- [17] Gerhard Randers-Pehrson, Gary W. Johnson, Stephen A. Marino, Yanping Xu, Alexander D. Dymnikov, and David J. Brenner. The Columbia University sub-micron charged particle beam. *Nuclear Instruments and Methods in Physics Research, Section A: Accelerators, Spectrometers, Detectors and Associated Equipment*, 609(2-3):294–299, 2009. ISSN 01689002. doi: 10.1016/j.nima.2009.08.041. URL <http://dx.doi.org/10.1016/j.nima.2009.08.041>.
- [18] M Heiss, BE Fischer, and Marian Cholewa. Status of the gsi microbeam facility for cell irradiation with single ions. *Radiation Research*, 161:87–119, 2004.
- [19] Ph Barberet, A. Balana, S. Incerti, C. Michelet-Habchi, Ph Moretto, and Th Pouthier. Development of a focused charged particle microbeam for the irradiation of individual cells. *Review of Scientific Instruments*, 76(1), 2005. ISSN 00346748. doi: 10.1063/1.1823551.

- [20] Yasuhiko Kobayashi, Tomoo Funayama, and Seiichi Wada. Irradiation of single mammalian cells with a precise number of energetic heavy ions – Applications of microbeams for studying cellular radiation response. *Nuclear Instruments and Methods in Physics Research B*, 210:308–311, 2003. doi: 10.1016/S0168-583X(03)01047-4.
- [21] Silvia Gerardi, Giuseppe Galeazzi, and Roberto Cherubini. A Microcollimated Ion Beam Facility for Investigations of the Effects of Low-Dose Radiation. *Radiation Research*, 164:586–590, 2005.
- [22] Charlotta Nilsson, Jan Pallon, Göran Thungström, Natalia Arteaga, Mikael Elfman, Per Kristiansson, Christer Nilsson, and Marie Wegdén. Characterisation of a pre-cell hit detector to be used in single cell irradiation experiments at the Lund Nuclear Microprobe. *Nuclear Inst. and Methods in Physics Research, B*, 266(21):4808–4815, 2008. ISSN 0168-583X. doi: 10.1016/j.nimb.2008.07.011. URL <http://dx.doi.org/10.1016/j.nimb.2008.07.011>.
- [23] Michael Grada, Andrew Harken, Daniel Attinger Gerhard Randers-Pehrsonb, and David J. Brenner. An ultra-thin Schottky diode as a transmission particle detector for biological microbeams. *Journal of Instrumentation*, 7(12):1–22, 2013. doi: 10.1088/1748-0221/7/12/P12001.An.
- [24] B E Fischer, M Heiß, and M Cholewa. About the art to shoot with single ions. *Nuclear Instruments and Methods in Physics Research B*, 210:285–291, 2003. doi: 10.1016/S0168-583X(03)01038-3.
- [25] N Arteaga-marrero, J Pallon, M G Olsson, V Auzelyte, and M Elfman. The

- new Cell Irradiation Facility at the Lund Nuclear Probe. 260:91–96, 2007. doi: 10.1016/j.nimb.2007.01.255.
- [26] P Golubev, P Kristiansson, M Elfman, K Malmqvist, E J C Nilsson, C Nilsson, J Pallon, and M Wegdén. Nuclear Instruments and Methods in Physics Research B First results from the Lund NMP particle detector system. *Nuclear Inst. and Methods in Physics Research, B*, 267(12-13):2065–2068, 2009. ISSN 0168-583X. doi: 10.1016/j.nimb.2009.03.030. URL <http://dx.doi.org/10.1016/j.nimb.2009.03.030>.
- [27] Alan Bigelow, Guy Garty, Tomoo Funayama, Gerhard Randers-pehrson, David Brenner, Charles Geard, and Microbeam Particle. Expanding the Question-answering Potential of Single-cell Microbeams at RARAF, USA. *Journal of Radiation Research*, 50(Suppl\_A):8–12, 2009. doi: 10.1269/jrr.08134S.
- [28] Tomas Richard Urlich. *DESIGN AND CONSTRUCTION OF A SILICON SCHOTTKY DIODE DETECTOR FOR SINGLE PROTON COUNTING AT THE MCMASTER MICROBEAM LABORATORY*. PhD thesis, 2017.
- [29] Xin Tong. *Development of a Thin CVD Diamond Detector as a Transmission-Type Alpha Particle Counter at McMaster University Biological Microbeam Facility*. PhD thesis, 2018.
- [30] Veljko Grilj, Natko Skukan, Milko Jakšić, M Pomorski, W Kada, T Kamiya, and T Ohshima. The evaluation of radiation damage parameter for cvd diamond. *Nuclear Instruments and Methods in Physics Research Section B: Beam Interactions with Materials and Atoms*, 372:161–164, 2016.

- [31] Hugh O Pierson. *Handbook of carbon, graphite, diamonds and fullerenes: processing, properties and applications*. William Andrew, 2012.
- [32] AR Lang and G Pang. On the dilation of diamond by nitrogen impurity aggregated in a defects. *Philosophical Transactions of the Royal Society of London. Series A: Mathematical, Physical and Engineering Sciences*, 356(1741):1397–1419, 1998.
- [33] Veronique Vermeeren, Sylvia Wenmackers, Patrick Wagner, and Luc Michiels. Dna sensors with diamond as a promising alternative transducer material. *Sensors*, 9(7):5600–5636, 2009.
- [34] P. Hofmann. *Solid State Physics: An Introduction*. Physics textbook. Wiley, 2011. ISBN 9783527657070. URL <https://books.google.ca/books?id=ShnfomzkPKQC>.
- [35] Karlheinz Seeger. *Semiconductor physics*. Springer Science & Business Media, 2013.
- [36] GS Painter, Donald E Ellis, and AR Lubinsky. Ab initio calculation of the electronic structure and optical properties of diamond using the discrete variational method. *Physical Review B*, 4(10):3610, 1971.
- [37] Glenn F Knoll. *Radiation detection and measurement*. John Wiley & Sons, 2010.
- [38] Ricardo S Sussmann. *CVD diamond for electronic devices and sensors*, volume 26. John Wiley & Sons, 2009.

- [39] DJ Twitchen, CSJ Pickles, SE Coe, RS Sussmann, and CE Hall. Thermal conductivity measurements on cvd diamond. *Diamond and related materials*, 10 (3-7):731–735, 2001.
- [40] Jan Isberg. Transport properties of electrons and holes in diamond. *CVD Diamond for Electronic Devices and Sensors*, pages 29–48, 2009.
- [41] John J Quinn and Kyung-Soo Yi. *Solid state physics: principles and modern applications*. Springer Science & Business Media, 2009.
- [42] F Nava, C Canali, C Jacoboni, L Reggiani, and SF Kozlov. Electron effective masses and lattice scattering in natural diamond. *Solid State Communications*, 33(4):475–477, 1980.
- [43] Jan Isberg, Johan Hammersberg, Erik Johansson, Tobias Wikström, Daniel J Twitchen, Andrew J Whitehead, Steven E Coe, and Geoffrey A Scarsbrook. High carrier mobility in single-crystal plasma-deposited diamond. *Science*, 297 (5587):1670–1672, 2002.
- [44] M Pomorski, E Berdermann, A Caragheorgheopol, M Ciobanu, M Kiš, A Martemiyarov, C Nebel, and P Moritz. Development of single-crystal cvd-diamond detectors for spectroscopy and timing. *Physica status solidi (a)*, 203 (12):3152–3160, 2006.
- [45] Michal Pomorski, Benoit Caylar, and Philippe Bergonzo. Super-thin single crystal diamond membrane radiation detectors. *Applied physics letters*, 103(11): 112106, 2013.

- [46] Gerhard Lutz et al. *Semiconductor radiation detectors*, volume 40. Springer, 1999.
- [47] Gordon Davies. Basic properties of diamond: Phonon spectra, thermal properties, band structure. *CVD Diamond for Electronic Devices and Sensors*, pages 3–28, 2009.
- [48] William G Eversole. Synthesis of diamond, April 17 1962. US Patent 3,030,188.
- [49] John C Angus, Herbert A Will, and Wayne S Stanko. Growth of diamond seed crystals by vapor deposition. *Journal of Applied Physics*, 39(6):2915–2922, 1968.
- [50] Seiichiro Matsumoto, Yoichiro Sato, Masayuki Tsutsumi, and Nobuo Setaka. Growth of diamond particles from methane-hydrogen gas. *Journal of Materials Science*, 17(11):3106–3112, 1982.
- [51] Mutsukazu Kamo, Yoichiro Sato, Seiichiro Matsumoto, and Nobuo Setaka. Diamond synthesis from gas phase in microwave plasma. *Journal of Crystal Growth*, 62(3):642–644, 1983.
- [52] Matsukazu Kamo, Hisayoshi Yurimoto, and Yoichiro Sato. Epitaxial growth of diamond on diamond substrate by plasma assisted cvd. *Applied Surface Science*, 33:553–560, 1988.
- [53] D Das and RN Singh. A review of nucleation, growth and low temperature synthesis of diamond thin films. *International Materials Reviews*, 52(1):29–64, 2007.
- [54] T. A. Railkar, W. P. Kang, Henry Windischmann, A. P. Malshe, H. A. Naseem, J. L. Davidson, and W. D. Brown. Critical review of chemical

- vapor-deposited (CVD) diamond for electronic applications. *Critical Reviews in Solid State and Materials Sciences*, 25(3):163–277, 2000. ISSN 10408436. doi: 10.1080/10408430008951119.
- [55] V. P. Varnin, V. A. Laptev, and V. G. Ralchenko. The state of the art in the growth of diamond crystals and films. *Inorganic Materials*, 42(SUPPL. 1), 2006. ISSN 00201685. doi: 10.1134/S0020168506130012.
- [56] D. Das and R. N. Singh. A review of nucleation, growth and low temperature synthesis of diamond thin films. *International Materials Reviews*, 52(1):29–64, 2007. ISSN 09506608. doi: 10.1179/174328007X160245.
- [57] JE Butler, A Cheesman, and MNR Ashfold. Recent progress in the understanding of cvd growth of diamond. *CVD Diamond for Electronic Devices and Sensors*, pages 103–124, 2009.
- [58] J Achard, F Silva, A Tallaire, X Bonnin, G Lombardi, K Hassouni, and A Gicquel. High quality mpacvd diamond single crystal growth: high microwave power density regime. *Journal of Physics D: Applied Physics*, 40(20):6175, 2007.
- [59] Annemie Bogaerts, Maxie Eckert, Ming Mao, and Erik Neyts. Computer modelling of the plasma chemistry and plasma-based growth mechanisms for nanostructured materials. *Journal of Physics D: Applied Physics*, 44(17):174030, 2011.
- [60] Lothar Ley. 4 surface conductivity of diamond. In *CVD Diamond for Electronic Devices and Sensors*, pages 69–102. John Wiley & Sons, Ltd Chichester, UK, 2009.
- [61] Alan Owens. *Semiconductor radiation detectors*. CRC Press, 2019.

- [62] Kwan Chi Kao. *Dielectric phenomena in solids*. Elsevier, 2004.
- [63] Hiroshi Kawarada. Hydrogen-terminated diamond surfaces and interfaces. *Surface Science Reports*, 26(7):205–259, 1996.
- [64] E Kohn and A Denisenko. Doped diamond electron devices. In *CVD diamond for electronic devices and sensors*. 2009.
- [65] Yusuke Mori, Hiroshi Kawarada, and Akio Hiraki. Properties of metal/diamond interfaces and effects of oxygen adsorbed onto diamond surface. *Applied physics letters*, 58(9):940–941, 1991.
- [66] LM Porter, K Das, Y Dong, JH Melby, and AR Virshup. Contacts to wide-band-gap semiconductors. 2011.
- [67] K Das, V Venkatesan, K Miyata, DL Dreifus, and JT Glass. A review of the electrical characteristics of metal contacts on diamond. *Thin Solid Films*, 212(1-2):19–24, 1992.
- [68] David Andrew Evans, Owain Rhys Roberts, Alex Raymond Vearey-Roberts, David Philip Langstaff, DJ Twitchen, and M Schwitters. Direct observation of schottky to ohmic transition in al-diamond contacts using real-time photoelectron spectroscopy. *Applied Physics Letters*, 91(13):132114, 2007.
- [69] D. R. Kania, M. I. Landstrass, M. A. Plano, L. S. Pan, and S. Han. Diamond radiation detectors. *Diamond and Related Materials*, 2(5-7):1012–1019, 1993. ISSN 09259635. doi: 10.1016/0925-9635(93)90266-5.
- [70] William R Leo. *Techniques for nuclear and particle physics experiments: a how-to approach*. Springer Science & Business Media, 2012.

- [71] GJ Schmid, JA Koch, RA Lerche, and MJ Moran. A neutron sensor based on single crystal cvd diamond. *Nuclear Instruments and Methods in Physics Research Section A: Accelerators, Spectrometers, Detectors and Associated Equipment*, 527(3):554–561, 2004.
- [72] P. Bergonzo, D. Tromson, and C. Mer. Radiation detection devices made from CVD diamond. *Semiconductor Science and Technology*, 18(3), 2003. ISSN 02681242. doi: 10.1088/0268-1242/18/3/315.
- [73] E Berdermann and M Ciobanu. 10 cvd-diamond detectors for experiments with hadrons, nuclei, and atoms. *CVD Diamond for Electronic Devices and Sensors*, 26:227, 2009.
- [74] Alan T Collins. Detectors for uv and far uv radiation. *CVD Diamond for Electronic Devices and Sensors*, pages 165–83, 2009.
- [75] Yuki Sato, Hiroyuki Murakami, Takehiro Shimaoka, Masakatsu Tsubota, and Junichi H. Kaneko. Charge-collection efficiency of single-crystal CVD diamond detector for low-energy charged particles with energies ranging from 100 keV to 2 MeV. *Nuclear Instruments and Methods in Physics Research, Section A: Accelerators, Spectrometers, Detectors and Associated Equipment*, 834:218–222, 2016. ISSN 01689002. doi: 10.1016/j.nima.2016.08.020.
- [76] J Isberg, J Hammersberg, DJ Twitchen, and AJ Whitehead. Single crystal diamond for electronic applications. *Diamond and Related Materials*, 13(2):320–324, 2004.

- [77] Alison Mainwood. Point defects, impurities and doping. *CVD Diamond for Electronic Devices and Sensors*, pages 49–63, 2009.
- [78] C. Manfredotti. CVD diamond detectors for nuclear and dosimetric applications. *Diamond and Related Materials*, 14(3-7):531–540, 2005. ISSN 09259635. doi: 10.1016/j.diamond.2004.11.037.
- [79] CE Nebel, A Waltenspiel, M Stutzmann, M Paul, and L Schäfer. Persistent photocurrents in cvd diamond. *Diamond and Related Materials*, 9(3-6):404–407, 2000.
- [80] Yuki Sato, Takehiro Shimaoka, Junichi H. Kaneko, Hiroyuki Murakami, Mitsutaka Isobe, Masaki Osakabe, Masakatsu Tsubota, Kentaro Ochiai, Akiyoshi Chayahara, Hitoshi Umezawa, and Shinichi Shikata. Radiation hardness of a single crystal CVD diamond detector for MeV energy protons. *Nuclear Instruments and Methods in Physics Research, Section A: Accelerators, Spectrometers, Detectors and Associated Equipment*, 784:147–150, 2015. ISSN 01689002. doi: 10.1016/j.nima.2014.12.036. URL <http://dx.doi.org/10.1016/j.nima.2014.12.036>.
- [81] Werner Kern and Karen Reinhardt. *Handbook of Silicon Wafer Cleaning Technology*. Elsevier, 2018.
- [82] J. F. Ziegler, U. Littmark, and J. P. Biersack. *The stopping and range of ions in solids / J.F. Ziegler, J.P. Biersack, U. Littmark*. Pergamon New York, 1985. ISBN 008021603.
- [83] Ch Eppacher and D Semrad. Determination of stopping power for ions by

- backscattering from thin targets. *Nuclear Instruments and Methods in Physics Research Section B: Beam Interactions with Materials and Atoms*, 35(2):109–117, 1988.
- [84] A General Monte Carlo N-Particle. Transport code. *MCNP homepage: <https://mcnp.lanl.gov>*, 2013.
- [85] Ronald J McConn, Christopher J Gesh, Richard T Pagh, Robert A Rucker, and Robert Williams III. Compendium of material composition data for radiation transport modeling. Technical report, Pacific Northwest National Lab.(PNNL), Richland, WA (United States), 2011.
- [86] Syed Naeem Ahmed. 2 - interaction of radiation with matter. In Syed Naeem Ahmed, editor, *Physics and Engineering of Radiation Detection (Second Edition)*, pages 65 – 155. Elsevier, second edition edition, 2015. ISBN 978-0-12-801363-2. doi: <https://doi.org/10.1016/B978-0-12-801363-2.00002-4>. URL <http://www.sciencedirect.com/science/article/pii/B9780128013632000024>.
- [87] Multiparametric D A Q Software and Physics Applications. CoMPASS Quick Start. 2020.
- [88] Ettore Vittone. Semiconductor characterization by scanning ion beam induced charge (ibic) microscopy. *International Scholarly Research Notices*, 2013, 2013.